


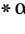

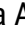











Crystal cargo perspectives on magma assembly and dynamics during the 2021 Tajogaite eruption, La Palma, Canary Islands

 Katy J. Chamberlain^{*α},  Matthew J. Pankhurst^{β,γ,δ},  David A. Neave^ε,  Daniel J. Morgan^ζ,
 Olivia A. Barbee^η,  Jane H. Scarrow^θ,  James Hickey^ι,  Sam Broom-Fendley^ι,  Joe Gardner^α,
 Gavyn K. Rollinson^ι, Richard Walshaw^ζ,  Alexander G. Stewart^ε,  Penny E. Wieser^κ,
 Beverley C. Coldwell^{β,γ},  Alba Martín-Lorenzo^{β,γ}, and  Fátima Rodríguez^β

^α Department of Earth, Ocean, and Ecological Sciences, School of Environmental Sciences, University of Liverpool, Liverpool, UK.

^β Instituto Volcanológico de Canarias (INVOLCAN); San Cristóbal de La Laguna, Tenerife, Spain.

^γ Instituto Tecnológico y de Energías Renovables (ITER), Granadilla de Abona, Tenerife, Spain.

^δ Now at: Gaiaxiom, Copenhagen, Denmark.

^ε Department of Earth and Environmental Sciences, University of Manchester, Manchester, UK.

^ζ School of Earth and Environment, University of Leeds, Leeds, UK.

^η Xnovo Technology, Køge, Denmark.

^θ Department of Mineralogy and Petrology, University of Granada, Granada, Spain.

^ι Department of Earth and Environmental Sciences, University of Exeter, Penryn, UK.

^κ Department of Earth and Planetary Science, University of California, Berkeley, CA, USA.

ABSTRACT

The 2021 Tajogaite eruption was the longest and most voluminous in recorded history on La Palma, Canary Islands. Extensive geophysical and geochemical data were collected before and during the eruption; however petrological monitoring saw little usage, largely restricted to rapid stereo microscope observations or off-island analyses. Here, we analyse lava and tephra sampled at near-daily frequency to investigate magmatic processes driving petrological, geochemical, and geophysical variations. Published whole-rock major and trace element data are combined with new QEMSCAN textural and mineral abundance data, major element analyses of macrocryst phases, and clinopyroxene trace element data, supported by mineral growth pressure–temperature modelling. Olivine Fe-Mg diffusion timescales from early tephra are compared with timescales of climactic unrest. Results indicate that more-evolved, mineralogically diverse magmas were tapped during the first week. Magma mixing only becomes apparent when more primitive magmas erupted after the first ~10 days, exemplified by reverse-zoned olivines. Clinopyroxene barometry suggests most material is fed from the upper mantle throughout. Timescales overlap and extend climactic unrest records, suggesting that destabilisation began before geophysical detection. From Stage 2 (~5–10 days) to eruption cessation (~85 days), crystal cargo chemistry is surprisingly uniform, with previously observed whole-rock and tephra glass changes not obviously reflected in the mineral record. We highlight the importance of combining both whole-rock and mineral scale observations to understand how eruptions progress, and ultimately end.

RESUMEN

La erupción de Tajogaite de 2021 fue la de mayor duración y la más voluminosa en la historia registrada en La Palma, Canarias. Se recogieron numerosos datos geofísicos y geoquímicos tanto antes como durante la erupción; sin embargo, el monitoreo petrológico fue poco utilizado, y se restringió principalmente a observaciones rápidas con microscopio estereoscópico o análisis fuera de la isla. En este trabajo, analizamos lava y tefra muestreadas con frecuencia casi diaria para investigar los procesos magmáticos responsables de los cambios petrológicos, geoquímicos y geofísicos. Combinamos datos publicados de elementos mayores y traza en roca total con nuevos datos texturales y de abundancia mineral obtenidos mediante QEMSCAN, análisis de elementos mayores de fases macrocristalinas y datos de elementos traza en clinopiroxeno, respaldados por modelos de presión y temperatura del crecimiento mineral. Las escalas de tiempo de difusión Fe-Mg en olivino de las primeras tefras se comparan con las del periodo de mayor inestabilidad. Los resultados indican que durante la primera semana se emitieron magmas más evolucionados y con mayor diversidad mineralógica. La mezcla de magmas solo se hace evidente cuando los magmas más primitivos fueron emitidos después de ~10 días, ejemplificada por olivinos con zonación inversa. La barometría en clinopiroxeno sugiere que la mayor parte del material fue alimentado desde el manto superior durante toda la erupción. Las escalas de tiempo se superponen y extienden con el registro de inestabilidad, lo que sugiere que la desestabilización comenzó antes de la detección geofísica. Desde la Etapa 2 (~5–10 días) hasta cese de la erupción (~85 días), la química de los cristales es sorprendentemente uniforme, y los cambios previamente observados en roca total y vidrio no se reflejan claramente en el registro mineral. Destacamos la importancia de combinar observaciones tanto a escala de roca total como a escala mineral para comprender cómo progresan, y finalmente terminan, las erupciones.

KEYWORDS: Tajogaite eruption; Canary Islands; Petrological monitoring; Eruption dynamics.

1 INTRODUCTION

The societal impacts of long-lived (> few days) mafic eruptions are often significant, wide-ranging, and dynamic, despite

*✉ k.j.chamberlain@liverpool.ac.uk

appearing less catastrophic than historic large-scale (yet comparatively very short-lived) explosive felsic eruptions. With eruption longevity also comes the opportunity to better understand magma plumbing system dynamics because knowing when, and in what order, material exits a system, places important constraints upon petrogenetic models. To better mitigate the impacts of long-lived eruptions, we must understand how magma ascent pathways and the evolution of magmas might influence longevity and eruptive style. Yet, geophysical and geochemical signals (measurable prior to eruption initiation, and available in near-real-time) can only reveal some magmatic processes through indirect observations of phenomena produced by magma ascent (e.g. changes in species and abundances of gas emissions, seismicity, ground deformation). In order to fully understand how magmas evolve (and thus the potential styles of eruption) both before and during eruptive episodes, geophysical and geochemical signals must be combined with petrological and geochemical assessments of erupted products, providing direct observations of magma ascent [Cassidy et al. 2018; Re et al. 2021]. Petrology is hindered with respect to eruption forecasting, as it necessitates the eruption having begun to provide material to analyse. Yet the value in petrological study of volcanic products is highlighted when eruptive behaviour is prolonged, and has the potential to help understand how and when eruptions will end, another vital question during volcanic crises [e.g. Gansecki et al. 2019; Re et al. 2021; Bindeman et al. 2022; Corsaro and Miraglia 2022; Halldórsson et al. 2022; Scarrow et al. 2024]. Therefore, by coupling geophysical, geochemical, and petrological studies of recent periods of volcanic activity, a more complete picture of how magmas assemble, ascend, and erupt—and how eruptions are sustained and ultimately end—may be achieved.

Ocean island provinces with high magma flux, such as Hawai'i, Iceland, and the Galápagos, are dominated by mafic eruption products and commonly experience extended periods of eruptive activity [e.g. Thordarson and Larsen 2007; Poland et al. 2008; Bernard et al. 2019]. For example, recent activity in 2021, 2022, and 2023 in Fagradalsfjall, Iceland, lasted for 184, 19, and 27 days respectively [GVP 2025]. During these periods, whilst activity is typically effusive to only weakly explosive, it becomes important to forecast not just the start of eruptive activity, but also its end. These styles of eruptions typically present low risk to life, yet have extensive destructive effects on land use, and are costly to recover from. For example, the 2018 Kilauea eruption triggered the evacuation of more than 3000 people, destroyed 723 buildings, and recovery will cost >\$800M USD [Houghton et al. 2021; Meredith et al. 2024]. The Canary Islands are another example of dominantly mafic, ocean island volcanoes, though with a relatively low magmatic flux when compared with Hawai'i and others. They are a key natural laboratory to integrate across various sub-disciplines, having experienced multiple eruptions in historic times, including the 2021 Tajogaite eruption [e.g. Carracedo et al. 1998; 1999; Bonadonna et al. 2022; Pankhurst et al. 2022; Ubide et al. 2023; Longpré et al. 2025].

Petrological study of erupted products has the potential to deconvolve subsurface magmatic processes in the lead up to, and during, eruptive episodes, that can sometimes be masked

when only considering whole-rock chemical compositions or geophysical and geochemical monitoring data [e.g. Corsaro and Miraglia 2022; Weber et al. 2024]. Crystals in volcanic products are scientifically valuable as they directly record dynamic magmatic processes that are otherwise inaccessible, and as such have been examined for decades, and in ever-increasing detail using a widening set of methods [e.g. Streck 2008]. Each crystal can be considered a microscale record of its own history experiencing local magmatic environments. Mineral compositions and textures can be used to infer pressures and temperatures of mineral growth/equilibria within magmatic plumbing systems [e.g. Barker et al. 2015; Halldórsson et al. 2018; Weber et al. 2024], interactions between different magma batches [e.g. Allan et al. 2013; Neave et al. 2014; Pizarro et al. 2019; Ruth and Costa 2021], and the timescales over which these pre- and syn-eruptive processes occurred [e.g. Morgan and Blake 2006; Chamberlain et al. 2014; Pankhurst et al. 2018; Conway et al. 2020; Kahl et al. 2022; Mangler et al. 2022; Ostorero et al. 2022]. Yet, due to questions of how significant and representative each crystal's record might be, extrapolation to macro-scale processes is non-trivial. Hence most crystal-scale studies search for populations and patterns using as many crystals as feasible when attempting to understand something of the system as a whole. Far rarer are studies that place crystal-scale observations within the context of an ongoing/evolving eruption [e.g. Pankhurst et al. 2018; Matthews et al. 2024], where the significance they may hold and interpretations they are used to construct might be independently tested. It is these verifiable links formed between petrological observation (applied to the products of any eruption in the rock record), and direct observation of volcanic processes of the same eruption (which cannot be made retrospectively), that have the greatest promise to better understand volcanic eruptions. This linkage between the past rock record and present-day monitoring of witnessed eruptions will allow us to both to interpret the past and plan for the future.

In this paper we present a time-series of mineral compositions, textures, intensive variables and timescales over the 85-day Tajogaite eruption on La Palma, in late 2021. By coupling mineral compositions, textures, and modelled information (temperatures, pressures, and timescales) to whole-rock compositions and observed geophysical signals, we highlight the advantages of detailed *in situ* mineral studies during eruptions. Additionally, we pinpoint the key analyses which could be prioritised in future periods of volcanic activity to better understand how eruptions progress. By integrating geophysical and geochemical insights into eruption progression, we can also refine the tuning of petrological monitoring of different systems [e.g. Re et al. 2021; Pankhurst et al. 2022].

2 GEOLOGICAL SETTING

La Palma is an intraplate volcanic island, and the most northwestern of the seven Canary Islands [Carracedo et al. 1998]. The Canary Islands developed on Jurassic oceanic crust [Schmincke et al. 1998], and weakly trend from oldest volcanic islands in the eastern sector of the island chain to younger volcanic islands in the western sector [Geldmacher et al. 2005],



leading some authors to suggest a mantle plume origin for the archipelago [e.g. Hoernle and Schmincke 1993]. However, historic eruptions are distributed across the entire ~500 km East–West spread of islands, which argues against a simple hotspot-track model.

The volcanism that created La Palma began ~4 Ma with an initial seamount phase lasting for ~1 Myr [Staudigel et al. 1986; Carracedo et al. 1999]. The first subaerial volcanism is preserved in the north of the island where the shield volcano of Taburiente, and subsequent edifices of Bejenado and Cumbre Nueva were active from ~1.7 Ma to ~410 ka (Figure 1). The youngest, and historically active, edifice of Cumbre Vieja (125 ka to present) encompasses the southern section of La Palma [Day et al. 1999; Carracedo et al. 2001; Barker et al. 2015]. Cumbre Vieja has produced eight historically recorded eruptions (Figure 1), with vents aligned roughly north-south along, and below, the axial ridge of the Cumbre Vieja complex [Carracedo 1994]. The Cumbre Vieja complex is dominantly composed of silica-undersaturated alkaline mafic lava flows and scoria cones, with rare but evenly dispersed evolved plugs and flows [Klügel et al. 2005, Figure 1]. Cumbre Vieja rocks range from basanite/tephrite to phonolite; common mineral phases are clinopyroxene, olivine ± titaniferous amphibole in mafic products, and amphibole + clinopyroxene + hauyne + apatite + plagioclase in more evolved magmas [Carracedo et al. 2001; Carracedo and Troll 2016].

The 2021 eruption began on the 19th of September, lasted for 85 days (to 13th December), and produced the Tajogaite scoria cone complex, lava field, and tephra blanket. Prior to eruption initiation, unrest occurred periodically for ~4 years with deep (15–35 km) seismic swarms and changes in gas emissions [Torres-González et al. 2020; Fernández et al. 2021; Padrón et al. 2022]. In the week prior to eruption, intense and migrating seismic unrest and ground deformation occurred [Carracedo et al. 2022; Civico et al. 2022; Romero et al. 2022; Wadsworth et al. 2022]. The eruption commenced explosively and sustained a tephra column, which developed into a NW–SE trending fire-fountaining fissure ~500 m long that fed lava flows. Up to six vents were active at various stages during the eruption, with NW vents more associated with lava flows and passive degassing, whereas SE vents were mostly associated with tephra plumes and lava fountains [Bonadonna et al. 2022; Romero et al. 2022]. Strombolian activity resulted in a ~12 km² lava field being emplaced on the west side of the island, and ~2.3 × 10⁷ m³ of tephra being deposited over the island and sea [Bonadonna et al. 2022]. As a result of the sustained eruption, more than 7500 people were evacuated, and 2800 buildings were destroyed or damaged [Bonadonna et al. 2022; Carracedo et al. 2022]. Studies have already been undertaken on the geophysical [e.g. D'Auria et al. 2022; Piña-Varas et al. 2023; Suarez et al. 2023], geochemical [e.g. Day et al. 2022; González-García et al. 2023; Ubide et al. 2023], and physical volcanology aspects of the eruption [e.g. Bonadonna et al. 2022; Di Fiore et al. 2023; Taddeucci et al. 2023], with a detailed time-series study of lava and tephra whole-rock compositions [Scarrou et al. 2024] highlighting three key phases within the eruption defined by correlated changes in magma compositions, geophysical observations, and eruptive phenomena.

3 SAMPLES AND METHODS

Following whole-rock analysis [see Scarrou et al. 2024], key samples were selected from across the entire duration of the eruptive sequence for textural and in situ mineralogical analyses. Twenty-nine samples of lava, including the earliest and latest accessible erupted material, alongside five samples of tephra were selected for imaging and diffusion modelling (Table 1). Aliquots of samples were cut into thick sections at the Universidad de Granada, Spain, and polished to 0.25 µm for textural analysis.

Quantitative Evaluation of Materials by Scanning Electron Microscopy (QEMSCAN®) analysis of thick sections was undertaken at the Camborne School of Mines, University of Exeter, UK using a QEMSCAN® 4300 [Gottlieb et al. 2000]. iMeasure v4.2SR1 and iDiscover 4.2SR1 and 4.3 [Rollinson et al. 2011] were used for sample measurement and data processing. The QEMSCAN® operated at 25 kV, 5 nA, a 1000 X-ray count rate per pixel, a working distance of around 22 mm under high vacuum and with beam calibration every 30 minutes. Sample measurement used the fieldscan measurement mode [Pirrie and Rollinson 2011] to analyse the samples at an X-ray resolution/pixel spacing of either 5 or 10 µm and a 1000 µm² field size (×68 magnification). QEMSCAN® data were processed to produce a phase map and an olivine composition map per sample, in which each distinct phase/composition was assigned an 8-bit pixel intensity value. Olivine compositions were divided into four equal ranges of forsterite content (using the Fe–Mg ratio in the raw data) which were later calibrated using Electron Probe Microanalysis (EPMA) data (see next paragraph). Pixels that did not fit the strict raw data requirements needed to be assigned a mineral phase were assigned to “Undifferentiated groundmass”, and instead reflect pixels containing glass or a combination of minerals ± glass below the pixel resolution. Isolated pixels of chemically complex phases may be the result of partial- or sub-volume interaction and not a true representation of phase abundance. Isolated and small clusters of QEMSCAN® pixels of amphibole were shown by back-scatter electron (BSE) data to be particularly prone to these effects, and so were added to the groundmass. Individual phase maps were extracted, labelled, and analysed in Python using the `pandas`, `numpy`, and `skimage` libraries. We chose an area of 10,000 µm² to reflect the minimum size of macrocrysts, and assigned every region smaller than this limit to the groundmass. Pixel connectivity was determined as any of four neighbours, as opposed to eight neighbours (any adjacent pixel including on the corners), which was found to be more accurate in delineating groundmass crystals from each other and so minimising clusters of groundmass crystals being assigned to the macrocryst classification. We estimate the abundance of macrocrysts to be accurate within 5%, as the styles of groundmass crystal clustering from phase to phase, and watershed parameters needed to separate them generate slightly differing results. An exhaustive methodological description is outside the scope of this work because, for our purposes of tracking possible changes across the eruption, any changes in data reduction method (which is applied to all samples at the same time) do not change the trends or interpretation. Phases that contributed ≥5% macrocrysts by area

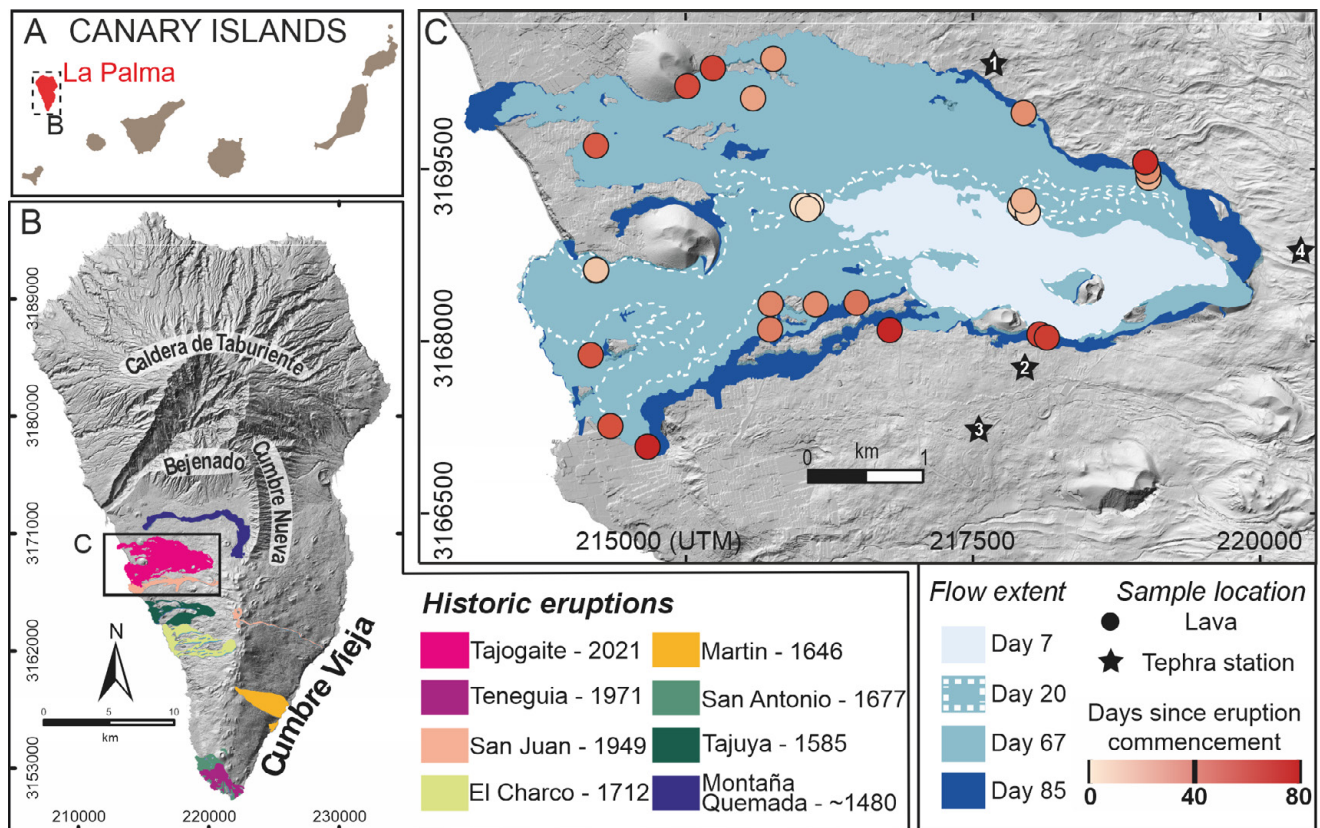


Figure 1: [A] Location of La Palma in the Canary Islands archipelago; [B] Location and extent of historic eruptions on La Palma showing the focus of activity along the Cumbre Vieja ridge. Tajogaite 2021 eruption: [C] Lava field extent by varying shades of blue; lava sample locations – circles, coloured by eruption date – and tephra collection pit locations – numbered black stars. Many sample sites were inundated by later flows. Modified from [Scarrow et al. \[2024\]](#).

(all area values are normalised to solid rock area) in at least one sample were categorised as “major”, while the rest were categorised as “minor”. Full details of the QEMSCAN® methodology can be found in [Supplementary Material 1](#).

Following QEMSCAN® analysis, key mineral species (olivine, clinopyroxene, amphibole) were identified and major element analyses were obtained by EPMA using a JEOL JXA 8230 instrument at the University of Leeds, using wavelength-dispersive spectrometry. Analytical conditions varied depending on the phase being analysed. Tephra matrix glass major and minor element concentrations were analysed from five key samples spanning eruptive days 3–80+, only totals between 98 and 102 wt.% were accepted as reliable, and normalised to 100 wt.% for comparison with existing glass data. For full details of conditions and precision and accuracy of EPMA data see [Supplementary Material 2](#).

Olivine EPMA spots were co-located in the QEMSCAN® data and used to build a 38-point calibration (see [Supplementary Material 1](#)) that returns an R^2 value of 0.98 from a linear regression. This calibration provides compositional quantification of the olivine distribution using the much larger QEMSCAN® dataset. The spots used for calibration were selected to span a range of Fo values (78.6–84.7 from a full dataset range of 78.1–85.9) and located within homogeneous core regions of olivine as observed from image analysis of QEMSCAN® and BSE images (see [Pankhurst et al. \[2018, 2019\]](#) for EPMA-BSE cal-

ibration methods). QEMSCAN pixel values from these regions were measured using ImageJ, where 1 is the most forsteritic range and 4 the most fayalitic, and the averaged values' standard error of the mean provides a measure of uncertainty. The number of pixels considered at each location varied from 26 to 5974 and an average of 710, according to the textural context. Larger crystal cores allowed for more pixels to be considered. Each QEMSCAN composition range is shown to be equivalent to ~2 Fo units (see [Supplementary Material 1](#)).

Clinopyroxene trace element concentrations were measured from seven samples by laser ablation inductively coupled plasma mass spectrometry (LA-ICP-MS) at the Camborne School of Mines, University of Exeter, using a New Wave Research 213 nm Nd-YAG laser coupled to an Agilent 7700 ICP-MS. The laser was operated using a 50 μm spot, 40 s dwell time and a repetition rate of 10 Hz, and a fluence of 3–4 J cm^{-2} . Data reduction was carried out using Iolite version 2.5 [\[Paton et al. 2011\]](#). Median ^{29}Si concentrations for pyroxene cores and rims, as obtained by EPMA, were used as the internal standard composition and NIST SRM 610 was used for calibration. Repeat analyses of reference materials BCR-2G and GSD-2G demonstrate the concentrations of almost all analysed elements fall within 10 % of published values (see [Supplementary Material 2](#)). Clinopyroxene targets were selected at random from the analyses of macrocrysts already characterised by EPMA.

Table 1: Studied sample locations, names and eruption times from lava and tephra of the 2021 Tajogaite eruption, La Palma.

Sample ID	Sample type	Date ^a	Time ^b	Latitude	Longitude	Days elapsed of eruption	Error (days)
CAN-LLP-0001	Lava	20/09/2021	02:00	28.619	−17.885	0.4	1
CAN-LLP-0003	Lava	22/09/2021	19:00	28.619	−17.904	3.2	0.02
CAN-LLP-0007	Lava	24/09/2021	12:00	28.618	−17.904	4.9	0.5
CAN-LLP-0011	Lava	26/09/2021	18:40	28.618	−17.884	7.2	0.02
CAN-LLP-0013	Lava	28/09/2021	08:15	28.613	−17.923	8.7	0.5
CAN-LLP-0014	Lava	29/09/2021	08:00	28.613	−17.923	9.7	0.5
CAN-LLP-0015	Lava	01/10/2021	15:30	28.619	−17.885	12	0.02
CAN-LLP-0016	Lava	02/10/2021	20:00	28.621	−17.874	13.2	0.02
CAN-LLP-0017	Lava	04/10/2021	12:00	28.619	−17.885	14.9	0.5
CAN-LLP-0019	Lava	07/10/2021	00:00	28.619	−17.904	17.4	0.5
CAN-LLP-0027	Lava	14/10/2021	19:30	28.627	−17.909	25.2	0.02
CAN-LLP-0033	Lava	19/10/2021	19:50	28.63	−17.907	30.2	0.02
CAN-LLP-0038	Lava	24/10/2021	12:00	28.622	−17.874	34.9	0.5
CAN-LLP-0041	Lava	24/10/2021	12:00	28.626	−17.885	34.9	0.5
CAN-LLP-0042	Lava	28/10/2021	17:00	28.611	−17.903	39.1	0.02
CAN-LLP-0046	Lava	29/10/2021	19:00	28.611	−17.907	40.2	0.02
CAN-LLP-0047	Lava	30/10/2021	13:30	28.609	−17.907	40.9	0.02
CAN-LLP-0049	Lava	02/11/2021	12:00	28.611	−17.899	43.9	0.5
CAN-LLP-0068	Lava	09/11/2021	17:00	28.607	−17.923	51.1	0.02
CAN-LLP-0070	Lava	11/11/2021	12:09	28.607	−17.923	53.9	0.01
CAN-LLP-0075	Lava	15/11/2021	17:40	28.601	−17.921	57.1	0.02
CAN-LLP-0077	Lava	21/11/2021	12:00	28.628	−17.915	62.9	0.5
CAN-LLP-0079	Lava	23/11/2021	13:00	28.629	−17.913	64.9	0.02
CAN-LLP-0081	Lava			28.608	−17.883	66.4	0.25
CAN-LLP-0082	Lava	25/11/2021	00:00	28.609	−17.883	66.4	0.5
CAN-LLP-0084	Lava	25/11/2021	17:45	28.609	−17.882	67.1	0.01
CAN-LLP-0094	Lava	01/12/2021	00:00	28.609	−17.896	72.37	1
CAN-LLP-0089	Lava	02/12/2021	12:15	28.623	−17.874	73.9	0.01
CAN-LLP-0096	Lava	07/12/2021	12:00	28.599	−17.918	78.9	1
CAN-TLP-0008	Tephra_AS1	22/09/2021	24 hours	28.624 518	−17.8847	2.78	-
CAN-TLP-0015	Tephra_AS3	26/09/2021		28.601 380	−17.8882	6.91	-
CAN-TLP-0034	Tephra_AS2	03/10/2021	24 hours	28.606 520	−17.8829	14.17	-
CAN-TLP-0099	Tephra_AS2	15/10/2021	24 hours	28.606 520	−17.8829	25.86	-
CAN-TLP-0199	Tephra_AS2	04/11/2021	24 hours	28.606 520	−17.8829	45.94	-
CAN-TLP-0270	Tephra_AS2	18/11/2021	24 hours	28.606 520	−17.8829	60.05	-
CAN-TLP-0370	Tephra_AS2	02/12/2021	24 hours	28.606 520	−17.8829	74.11	-
CAN-TLP-0445	Tephra_AS4	LATE	-	28.612 596	−17.8625	-	-

^a Emplacement date.^b Emplacement time.

We performed thermobarometric calculations on clinopyroxene and amphibole compositions using EPMA data collected as part of this study as well as whole-rock and glass data from the 2021 Tajogaite eruption [Day et al. 2022; Scarrow et al. 2024; Longpré et al. 2025] and the 1971 Teneguía eruption [Klügel et al. 2005; Prægel and Holm 2006; Barker et al. 2015; Weis et al. 2015]. Clinopyroxene-liquid geothermobarometry was performed using the barometer of Neave and Putirka [2017] iterated with the thermometer presented in Equation 33 of Putirka [2008]. These models are associated with prediction uncertainties (expressed as standard errors of estimate (SEEs)) of 140 MPa and 27 °C, respectively when tested against their calibration datasets. Although the barom-

eter of Neave and Putirka [2017] was originally calibrated for use in tholeiitic systems, comparing our clinopyroxene and liquid (i.e. glass and whole-rock) compositions with the compositions used for model calibration demonstrate that it can be useful in moderately alkalic systems like the 2021 Tajogaite eruption (Supplementary Material 2).

Iterative clinopyroxene-liquid matching was performed using the thermobar Python package [Wieser et al. 2022]. Clinopyroxene compositions were matched to tephra glass compositions from the 2021 Tajogaite eruption on the basis that these represent true, if compositionally variable, magmatic liquids erupted from the plumbing system. Calculations were performed with three different barometer-thermometer

pairs to check for internal consistency: the barometer of [Neave and Putirka \[2017\]](#) paired with the thermometer presented in Equation 33 of [Putirka \[2008\]](#), the barometer presented in Equation 31 of [Putirka \[2008\]](#) paired with the thermometer presented in Equation 33 of [Putirka \[2008\]](#) and the P1 barometer of [Putirka et al. \[1996\]](#) paired with the T1 thermometer of [Putirka et al. \[1996\]](#). Ultimately we found that all three barometer-thermometer pairs returned equivalent results within uncertainty, and so present the results of calculations performed with the barometer of [Neave and Putirka \[2017\]](#) in the main text (results from all model pairs are provided in [Supplementary Material 2](#)).

Equilibrium clinopyroxene-liquid pairs were estimated in two ways that both assumed that all Fe was present as Fe^{2+} [e.g. [Wieser et al. 2023](#)]. Firstly, matches were identified following the a slightly modified approach of [Neave et al. \[2019\]](#): pairs were considered to be in equilibrium when they were within 1SEE of DiHd and EnFs equilibrium (± 0.06 and ± 0.05 , respectively) according to the models of [Mollo et al. \[2013\]](#), 1SEE of CaTs equilibrium (± 0.03) according to the model of [Putirka et al. \[1996\]](#) and 1SEE of $\text{Kd}^{(\text{Fe-Mg})}$ equilibrium (± 0.08) according to Equation 35 of [Putirka \[2008\]](#). Following this approach we found that analyses from low-Al hourglass sectors in clinopyroxene rims returned pressures ~ 500 MPa lower than analyses of high-Al prism sectors in the same rims. As such, Na partitioning between hourglass and prism sectors in clinopyroxene crystals from Tajogaite fundamentally affects thermobarometric calculations. Interestingly, offsets between sectors have been noted in some alkaline systems (e.g. Haleakala [[Hammer et al. 2016](#)]), but not others (e.g. Etna [[Ubide et al. 2019](#)]). As such we exclude analyses from sectors containing < 6.5 wt.% Al_2O_3 from subsequent discussions as they likely represent compositions formed during disequilibrium crystallisation [[Neave et al. 2019](#)]. Secondly, and to avoid imposing bias by excluding data based on a simple compositional filter, we identified matches following the approach of [MacDonald et al. \[2023\]](#): pairs were considered to be in equilibrium when they were within approximately 2SEE of DiHd equilibrium and 1SEE of EnFs equilibrium (± 0.10 and ± 0.05 , respectively) according to the models of [Mollo et al. \[2013\]](#), and 1SEE of CaTs and CaTi equilibrium according to the models of [Putirka et al. \[1996\]](#). Importantly, this approach appears to rigorously reject analyses from low-Al hourglass sectors, and returns, to first order, magma storage conditions within uncertainty (1SEE; ± 140 MPa and ± 27 °C) of those estimated with the approach of [Neave et al. \[2019\]](#).

Additional amphibole-only thermobarometry was performed using the barometer of [Ridolfi \[2021\]](#) and the thermometer of [Ridolfi and Renzulli \[2012\]](#). The quoted uncertainties for these methods are 12% relative and 22 °C, respectively, although tests on independent calibration datasets reveal larger errors [[Wieser et al. 2025](#)]. However, unlike clinopyroxene crystals that are found in products from throughout the eruption, analysable amphibole crystals were only found in products from the earliest days of the eruption, and thus provide a partial record of magmatic processes.

To undertake diffusion modelling, orientations of olivine mineral grains were determined by electron backscatter

diffraction (EBSD) methods using a FEI Quanta 650 Field Emission Gun-Environmental Scanning Electron Microscope (FEGSEM) at the University of Leeds, and the Zeiss Gemini 450 FEGSEM in the SEM Shared Research Facility at the University of Liverpool. Backscattered electron (BSE) images of zoned olivine grains were collected at the University of Derby (on a Tescan Vega 3 SEM) and the University of Liverpool (on a Zeiss Gemini 450 FEGSEM). Greyscale profiles of Fe-Mg in olivine were extracted from BSE images using ImageJ® software. The greyscale values were then tied to Mg# ($\text{Mg\#} = 100 \times \text{Mg} / [\text{Mg} + \text{Fe}]$) using analysed EPMA spots, and then modelled using AUTODIFF following the method of [Couperthwaite et al. \[2020\]](#). Seventeen crystals from a single tephra sample were used for diffusion modelling, at two temperatures of 1125 °C and 1150 °C, representing the systemic range in modelled clinopyroxene-melt thermometry, 860 MPa pressure, from clinopyroxene-melt barometry (above), and $f\text{O}_2$ at NNO+1 within the range of oxygen fugacities published on the Tajogaite eruptions [[Frascerra et al. 2024](#)] and from the previous two eruptions from La Palma with intensive variables from past eruptions [[Klügel 1998](#); [Klügel et al. 2005](#); [Barker et al. 2015](#)]. The range of past oxygen fugacities varies by ~ 3.0 log units, we have used a single value for a single sample; more oxidising conditions would result in shorter modelled timescales, more reducing conditions would result in longer modelled timescales. Each Mg# profile was extracted perpendicular to the imaged crystal edge, and the orientation of this profile relative to crystallographic axes (established from output Euler poles in EBSD analyses using the spreadsheet Eulerproc, available on request from DJM) was input into the AUTODIFF model to account for the known anisotropy of Fe-Mg interdiffusion in olivine [[Couperthwaite et al. 2020](#)]. Uncertainties on modelled timescales were calculated using a Monte Carlo simulation incorporating a ± 30 °C analytical uncertainty on temperatures, and associated uncertainties on true pixel size, the number of integrated pixel lines across each boundary, $f\text{O}_2$ uncertainty (± 0.3 log units), and the greyscale intensity used to define the Mg# values.

4 RESULTS

4.1 Whole-rock framework

It is clear from published data that magmas erupted during the Tajogaite eruption are exclusively silica-undersaturated mafic alkali basalts in composition [[Day et al. 2022](#); [Pankhurst et al. 2022](#); [Ubide et al. 2023](#); [Scarrow et al. 2024](#)]. Within this restricted compositional range and as a result of detailed time-series sampling, [Scarrow et al. \[2024\]](#) identified three key stages within the eruption progression based on temporal trends in whole-rock element concentrations and ratios. The identification of three stages is supported by other published data including radiogenic isotope work, geophysical data, and fluid inclusion data [[Figure 2 Day et al. 2022](#); [Dayton et al. 2023](#); [Ubide et al. 2023](#); [Scarrow et al. 2024](#); [Zanon et al. 2024](#)], and can be summarised as follows ([Figure 2](#)):

Stage 1

Eruption onset to \sim day 5: This stage is marked by significant changes in erupted magma compositions over a short

duration, with whole-rock MgO increasing between 6.0 and 6.7 wt.%, coupled with increases in Ni from 50 to 65 ppm, and decreasing Zr (355–340 ppm [Scarrou et al. 2024]). At this time, groundmass materials have highly radiogenic $^{87}\text{Sr}/^{86}\text{Sr}$ [Ubide et al. 2023] and radiogenic $^{187}\text{Os}/^{188}\text{Os}$ [Day et al. 2022].

Stage 2

~Day 7 to ~day 67: During this stage whole-rock MgO and Ni concentrations rise from 7.5 to 8.6 wt.% and from 85 to 130 ppm respectively [Scarrou et al. 2024]. This rise continues to ~day 18 when MgO (and coupled elements) plateaus, and the erupted magma compositions stabilise. The general increase and stabilisation in MgO is matched by Sr isotopic data, with a systematic trend from $^{87}\text{Sr}/^{86}\text{Sr}$ of ~0.70315 to ~0.70307 in the first ~half of the eruption. Ratios from the last ~half of the eruption are reported as forming two parallel trends at ~0.70312 and ~0.70304 [Ubide et al. 2023]. $^{187}\text{Os}/^{188}\text{Os}$ similarly stabilise at less radiogenic ratios [Day et al. 2022].

Stage 3

~Day 70 to eruption end: this stage is only evident in whole-rock and glass (and matrix) compositions, and is marked by an inflection and then decrease in MgO concentrations from 8.6 to 8.0 wt.% (alongside Ni, TiO_2 , and increases in K_2O , Al_2O_3 , Na_2O , Zr, Ba, Sr [Scarrou et al. 2024]). No change is evident in the existing radiogenic isotope data [Day et al. 2022; Ubide et al. 2023], which may be due to limited sample coverage for those data during this time period.

4.2 QEMSCAN

Products erupted in the first few days (i.e. Stage 1) host a polyminerallitic crystal cargo of clinopyroxene, amphibole, titanomagnetite, minor plagioclase, and rare olivine [Pankhurst et al. 2022]. Crystals occur as polyhedral clusters up to 3 mm in length as well as individual crystals up to 2 mm in most samples, with most (and all titanomagnetite and olivine) being <0.5 mm (Table 2, Figure 3). Products from Stages 2 and 3 are characterised by comparatively invariant abundances and textures of clinopyroxene and olivine up to a few mm in length, where the amount of plagioclase is sensitive to the degree of late-stage cooling experienced before quenching, discussed below. All samples exhibit a seriate texture (see Supplementary Material 1 for plots of crystal size distribution through time), and we find that $10,000\ \mu\text{m}^2$ is a useful distinction between macrocrysts and microcrysts to represent the variations in crystal sizes observed across all mineral phases. All percentages reflect areal % of examined thin sections. Figure 4A illustrates that macrocrystic olivine abundance increases from zero to 5% over the first ~10 days and then is stable at 5% (with maxima of 6.8 and minima of 3.6) for the remaining eruption duration. Likewise, clinopyroxene increases from 6.3% to 11.5% in the first ~10 days, and is also comparatively stable at 12.5% for the duration (varying between 17% and 9.7%).

Amphibole is reported by the QEMSCAN® protocol throughout the eruption in the groundmass and as visually identified macrocrysts in the earliest of samples and the very last (one fully recrystallised instance in sample CAN_LL0096, from day 79: Figure 3). The majority of pixels classified as

amphibole are single and isolated, which is below the spatial confidence threshold. These data points likely represent fine-grained clusters of other phases (i.e. clinopyroxene, plagioclase, ilmenite, glass) below the pixel resolution whose individual signals are convolved to approximate an amphibole composition (evident in some samples where BSE images were collected). Amphibole pixels in obvious clusters well above the spatial confidence threshold typically exhibit rounded margins and variably patchy interiors. They are most abundant in CAN_LL0003 (day 3 of the eruption) but do not exceed >0.5% by area when connectivity is based on four neighbours or >0.7% when based on eight neighbours. These clusters are interpreted as kaersutite [Pankhurst et al. 2022] that preliminary results suggest has been variably recrystallized to a combination of rhönite, plagioclase, clinopyroxene, and ilmenite. These results are the topic of further work that will not be discussed in greater detail here. In this contribution we show that these variably recrystallized amphibole clusters are only characteristic of the first few days of the eruption. We therefore consider macrocrystic amphibole (and/or its recrystallized products) to be a minor phase whose presence is a robust characteristic of Stage 1, and whose abundance decreases together with other petrological signals from Stage 1 to Stage 2. Titanomagnetite macrocrysts, like amphibole, are most abundant in Stage 1 (maximum 0.85%), and after a sharp decrease into Stage 2 (0.3%) steadily decrease throughout the eruption (Figure 4).

Plagioclase is a ubiquitous phase and present in abundances from 4 to 25%, yet is exceedingly rare as macrocrysts and its abundance is controlled almost completely by the degree of late-stage crystallisation. Its abundance comprises an average of 34% of the total microcryst percentage (minimum: 18%, maximum: 44%). When expressed as a percentage of the total microcryst abundance, plagioclase is confirmed as a very late crystallising phase, since those samples with the lowest amount of microcrysts (i.e. glassier groundmass) have disproportionately low plagioclase abundance (see Supplementary Material 1). Plagioclase macrocrysts are calculated as exceeding 1% of rock area in several samples (Figure 4), although this occurs only in samples where the total plagioclase is >20%, and many instances may be artefacts of lath clustering that eluded watershed segmentation rather than reflecting true individual macrocrysts. We struck a balance between the complexity of the segmentation protocol and its final accuracy, and found that using a simple watershed avoided the misattribution of plagioclase clusters to macrocrysts even in the most plagioclase-rich groundmasses.

Olivine trends from rare fayalitic ($\text{Fo} < 77.6$) and microcrystic (0.17% macrocrysts of rock area) to forsteritic and macrocrystic ($\text{Fo} > 83.2$, 4.57% by day 12) from Stage 1 into Stage 2, and then maintains a comparatively consistent abundance and texture until the end of eruption (see Figure 4 and Supplementary Material 1).

4.3 Mineral compositions

The compositional variation of macrocryst phases through eruption time are similarly restricted to that of their abundances and matches the timing of textural changes. In both

Table 2: Mineral phase abundances. All values are normalised to total rock area (calculated on a vesicle-free basis). Cpx = Clinopyroxene; Ol = Olivine; Plg = Plagioclase; Amp = Amphibole; Ilm = Ilmenite; Tmt = Ti-Magnetite; Cr-Spl = Chrome spinel; Rhoe = Rhönite; Ap = Apatite; Gp = Gypsum.

Sample ID	Days elapsed of eruption	Spatial resolution (µm)	Undifferentiated groundmass (%)	Crystals <100 µm (%)*	Macrocryst abundance (%)										Total phenocryst abundance (%)	
					Cpx	Ol	Plg	Amp	Ilm	Tmt	Cr-Spl	Rhoe	Ap	Gp	Others	
CAN-LIP-0001	0.4	5	44.72	47.66	6.18	0.17	0.06	0.35	0.01	0.86	0	0	0	0	0	7.63
CAN-LIP-0003	3.16	10	37.65	52.92	8.24	0.39	0.22	0.13	0.04	0.39	0	0	0.02	0.01	0	9.44
CAN-LIP-0007	4.87	10	37.76	53.72	6.91	0.33	0.18	0.33	0	0.77	0	0	0	0	0	8.52
CAN-LIP-0011	7.15	10	46.04	39.61	12.39	1.6	0.02	0	0.01	0.3	0.02	0	0.01	0	0	14.35
CAN-LIP-0013	8.71	10	37.35	49.38	10.37	2.36	0.15	0.11	0.01	0.23	0.01	0.03	0	0	0.01	13.28
CAN-LIP-0014	9.7	5	40.32	46.86	9.22	3.44	0.01	0	0	0.13	0	0.01	0	0	0	12.81
CAN-LIP-0015	12.01	10	41.29	42.55	11.08	4.57	0.05	0	0	0.41	0.01	0.02	0	0	0.02	16.16
CAN-LIP-0016	13.2	10	56.3	23.26	16.61	3.05	0.24	0.1	0	0.33	0.09	0	0.02	0	0	20.44
CAN-LIP-0017	14.87	10	44.95	41.9	9.41	3.39	0.02	0	0	0.31	0.02	0	0	0	0	13.15
CAN-LIP-0019	17.37	5	48.66	34.64	12.84	3.71	0	0	0	0.14	0.01	0	0	0	0	16.7
CAN-LIP-0027	25.18	10	26.44	56.46	9.14	6.75	0.94	0	0	0.22	0	0	0	0	0.04	17.09
CAN-LIP-0033	30.19	10	52.34	31.47	10.9	5.09	0.07	0	0	0.11	0.01	0	0	0	0	16.18
CAN-LIP-0038	34.87	10	42.31	42.01	10.94	4.5	0.05	0	0	0.12	0.01	0	0	0	0.07	15.69
CAN-LIP-0042_d1	39.08	5	35.72	49.42	10.77	3.78	0.06	0	0	0.19	0.02	0.03	0	0	0	14.85
CAN-LIP-0042_d2	39.08	5	34.86	49.49	11.52	3.89	0.04	0	0	0.11	0	0.02	0.01	0	0.05	15.64
CAN-LIP-0046	40.16	10	27.72	54.59	10.69	4.49	2.38	0	0	0.12	0.01	0	0	0	0	17.69
CAN-LIP-0047	40.93	10	36.48	48.1	11.71	3.56	0.05	0	0	0.1	0	0	0	0	0	15.42
CAN-LIP-0049	43.87	10	40.77	40.88	13.8	4.35	0.07	0	0	0.1	0	0	0	0	0.03	18.35
CAN-LIP-0068	51.08	10	36.41	45.88	10.2	6.79	0.55	0	0	0	0	0	0	0	0.17	17.71
CAN-LIP-0070	53.88	10	36.75	47.81	10.54	4.47	0.17	0	0	0.01	0	0	0.01	0.02	0.22	15.44
CAN-LIP-0075	57.1	10	24.21	59.54	8.91	4.8	2.26	0	0	0.18	0.02	0	0	0	0.09	16.26
CAN-LIP-0077	62.87	10	23.92	59.16	9.3	5.79	1.66	0	0	0.08	0.03	0	0	0	0.07	16.93
CAN-LIP-0079	64.91	10	23.47	58.96	10.62	5.29	1.63	0	0	0.01	0.02	0	0	0	0	17.57
CAN-LIP-0081	66.37	10	41.64	41.98	10.53	5.73	0.11	0	0	0	0	0	0	0	0	16.37
CAN-LIP-0082	66.37	10	46	38.61	10.85	4.32	0.22	0	0	0.01	0	0	0	0	0	15.4
CAN-LIP-0084	67.11	10	48.11	35.72	11.38	4.59	0.04	0	0	0.02	0.01	0	0	0	0.13	16.17
CAN-LIP-0094	72.37	10	54.75	29.53	11.29	4.4	0.03	0	0	0	0	0	0	0	0	15.72
CAN-LIP-0089	73.88	10	31.72	52.35	11.45	4.35	0.11	0	0	0.01	0	0	0.01	0	0	15.93
CAN-LIP-0096	78.87	10	29.87	47.28	15.15	4.97	2.44	0.03	0	0.05	0	0.01	0.02	0.01	0.17	22.85

* K-feldspar, Chlorite, Kaolinite, Biotite, Ti-Magnetite, Magnetite, Chrome spinel, Rhönite, Apatite, Gypsum, and Sulphides are all detected in the microcrystalline groundmass but do not exhibit any crystal <100 µm.

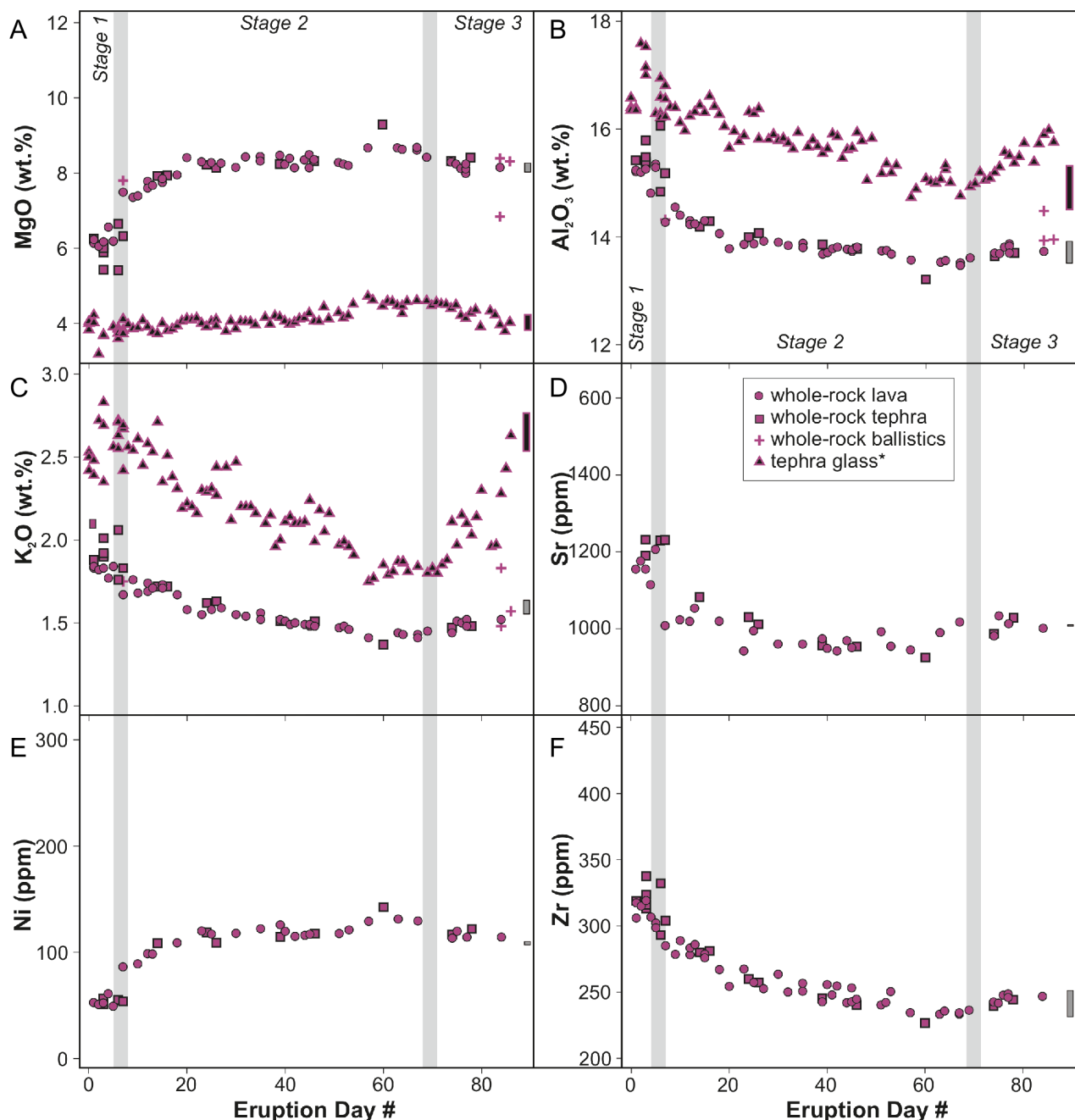


Figure 2: Published whole-rock major and trace element data from Scarrow et al. [2024] and tephra glass data (*) from Longpré et al. [2025]. Three identified stages from Scarrow et al. [2024] shown as grey vertical bars. Uncertainties on analyses are shown as the grey bars on the right side of graphs [Scarrow et al. 2024] or as black bars [Longpré et al. 2025].

tephra and lava samples, Stage 1 olivine cores and rims have generally much more restricted compositions than during the rest of the eruption sequence, with Fo 77.1–82.2 and NiO 0.03–0.19 wt.%. After Stage 1, olivine exhibits greater compositional diversity within individual samples, with Fo 70.5–85.9 and NiO between 0.05–0.30 wt.% (Figure 5A). Olivine cores either overlap with or are slightly more primitive than rim analyses in all samples (Figure 5B). There is no distinguishable difference in olivine compositions between Stage 2 and Stage 3. The

complete major and trace element mineral dataset is reported in Supplementary Material 3.

Clinopyroxene is the most abundant mineral phase throughout the Tajogaite eruption (Figure 4) and exhibits a considerable range in composition, yet no obvious differences in clinopyroxene core or rim major element compositions are evident through the eruption progression (Figure 6). Macrocrystic (>250 µm) clinopyroxene cores have diverse compositions with Mg# between 56 and 83, and TiO₂ concentrations in the range 0.85–4.84 wt.%. Rim and groundmass composi-

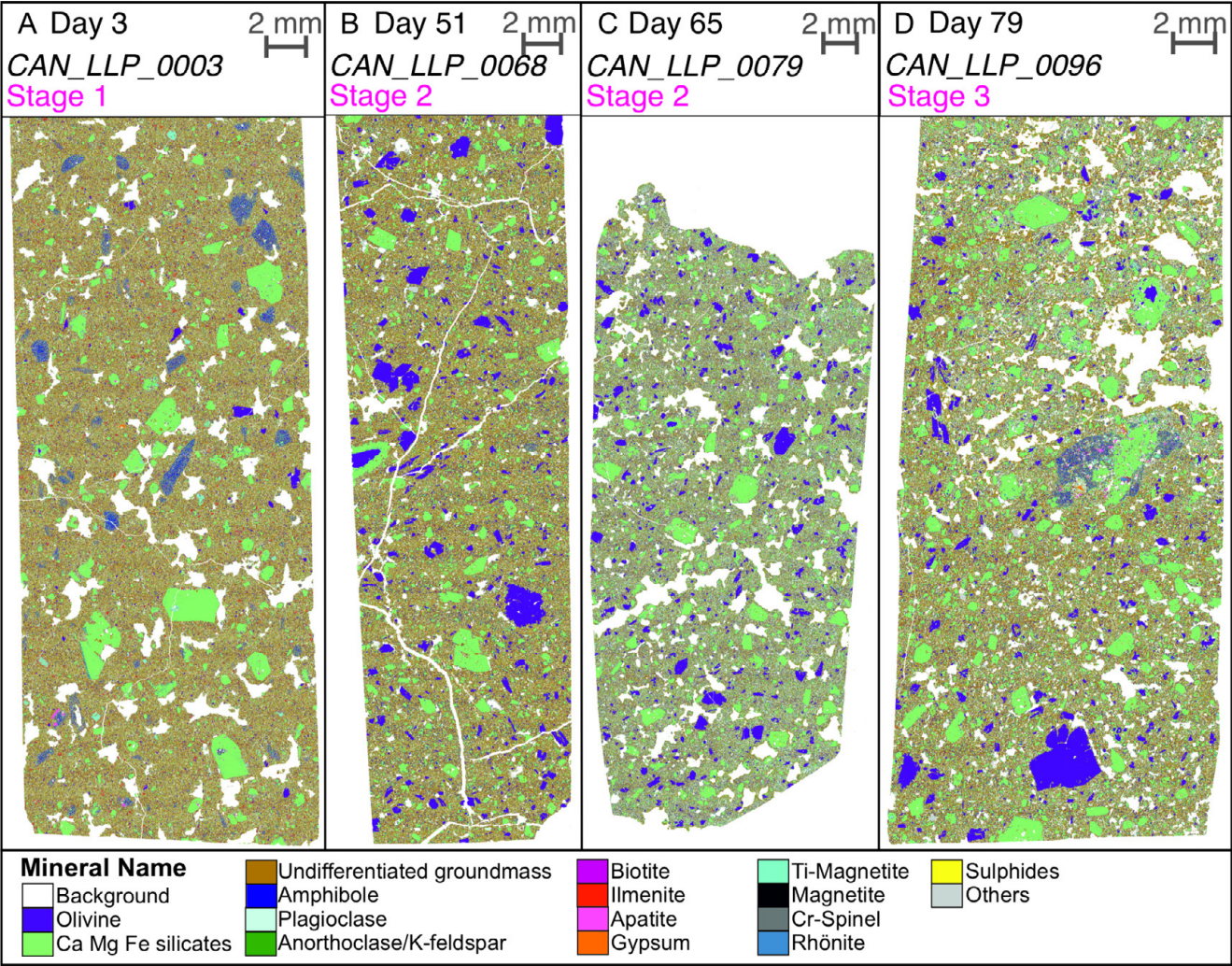


Figure 3: QEMSCAN® maps from Stage 1 [A], Stage 2 [B, C], and Stage 3 [D] lavas of the Tajogaite eruption. Clinopyroxene (light green) is the major macrocryst phase in all stages. Olivine becomes a major macrocryst phase from Stage 2. Amphibole occurs mainly as isolated macrocrysts in Stage 1 only, and is present only once again as part of one polymineralic cluster at the end of the eruption. Differences in groundmass texture (e.g. [B]: glassy vs [C]: microcrystalline) indicate the role that phase connectedness plays when calculating macrocryst percentages and underscores the importance of image segmentation. Inferred phases (see key) are a result of chemical identification using index-matching to the most likely minerals based on sample type, and confirmed by EPMA.

tions have similar compositions; Mg# ranges from 55 to 79 and TiO₂ between 1.75 and 6.71 wt.%. Similarly to the major element compositions, there are no clear trends in clinopyroxene trace element concentrations or ratios with eruption progression (Figure 6B, 6D). Stage 1 clinopyroxene cores span similar ranges in trace element concentrations to Stage 3 clinopyroxene. Stage 2 clinopyroxenes have similar trace element ranges, however the amount of variation within a single specimen varies between samples, which may reflect limited numbers of crystals analysed per sample.

In samples containing unaltered amphibole crystals (LLP_0001 and LLP_0003, from day 1 and day 3 of the eruption respectively), major element analyses show limited differences in amphibole compositions. Ti_(23O, apfu) ranges between 0.58 and 0.72, and Mg# (Mg_(23O, apfu)/[Mg_(23O, apfu)+Fe_(23O, apfu)]) between 0.62 and 0.72. These concentrations place the amphibole in the

kaersutite field (Figure 7A) and agree with the QEMSCAN® results. Amphiboles from day 3 of the eruptive sequence appear to have slightly higher Mg#s than those from day 1, but other major element concentrations (Ca, Na, Al(IV, apfu), Ti_(23O, apfu)) show substantial overlap between the two days (Figure 7).

Major and minor element concentrations of tephra glass were collected from 5 samples that span eruption days 3–80 (see Table 1 for sample details) and compared with existing glass average compositions from Longpré et al. [2025]. Individual glass analyses reported here overlap with the average tephra glass analyses from the entire eruption duration, with SiO₂ concentrations in the range 43.6 to 49.1 wt.%, Na₂O+K₂O 6.08–9.22 wt.% and MgO 3.4–5.9 wt.% (Figure 8). Earliest erupted tephra samples are the most evolved, with the highest SiO₂, total alkalis, and lowest MgO, FeO, and CaO/Al₂O₃. Tephra samples from day 60 are the least evolved of the sam-

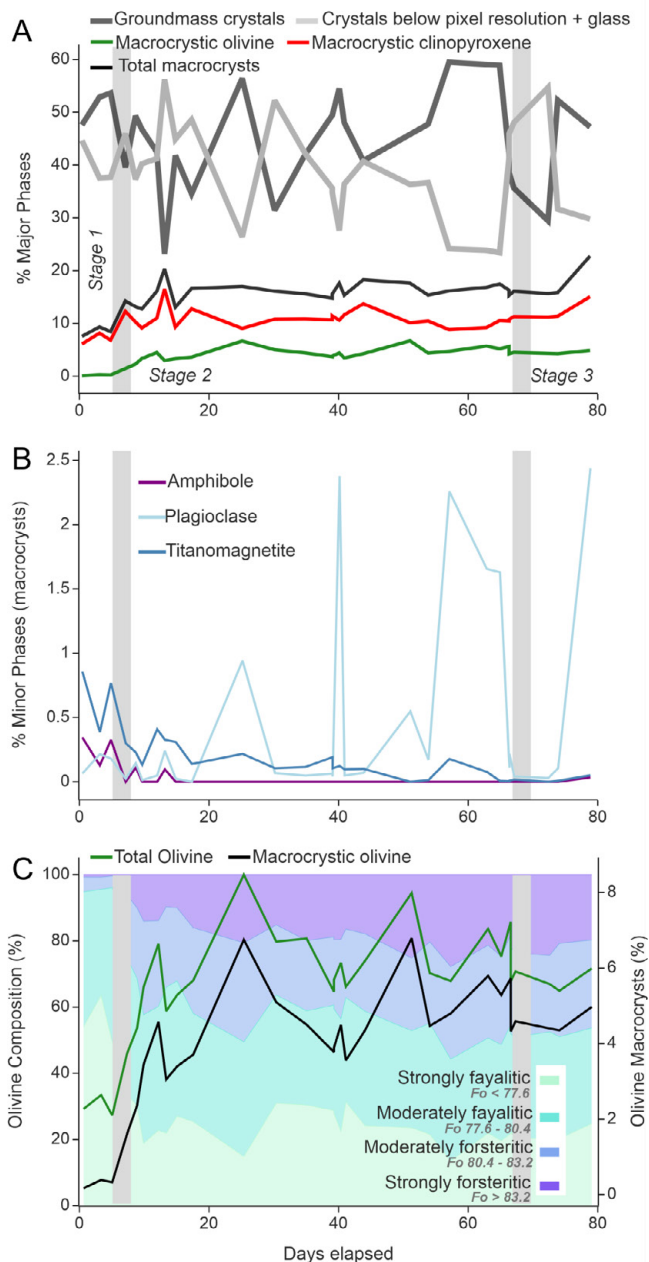


Figure 4: Temporal trends in mineral proportions and compositions during the Tajogaite eruption, as derived from QEMSCAN® analysis of lava samples, with key stages identified from [Scarrow et al. \[2024\]](#) shown as vertical grey bars. [A] Major mineral phases shown as macrocryst proportions (red, green and black, where macrocrysts refer to grains $>10,000 \mu\text{m}^2$); [B] Selected minor macrocryst phase abundance (for full phase variation see [Table 2](#)); [C] Olivine compositional change over the eruption shown as proportions (coloured zones), compared with both total olivine and macrocrystic olivine abundance (green and black lines, secondary y-axis).

ple analysed here, with tephra from day 80+ recording a slight increase in SiO_2 from day 60 ([Figure 8](#))—following whole-rock trends, where this change in SiO_2 is accompanied by a ~50% relative increase in K_2O in whole-rock analyses ([Figure 2](#)).

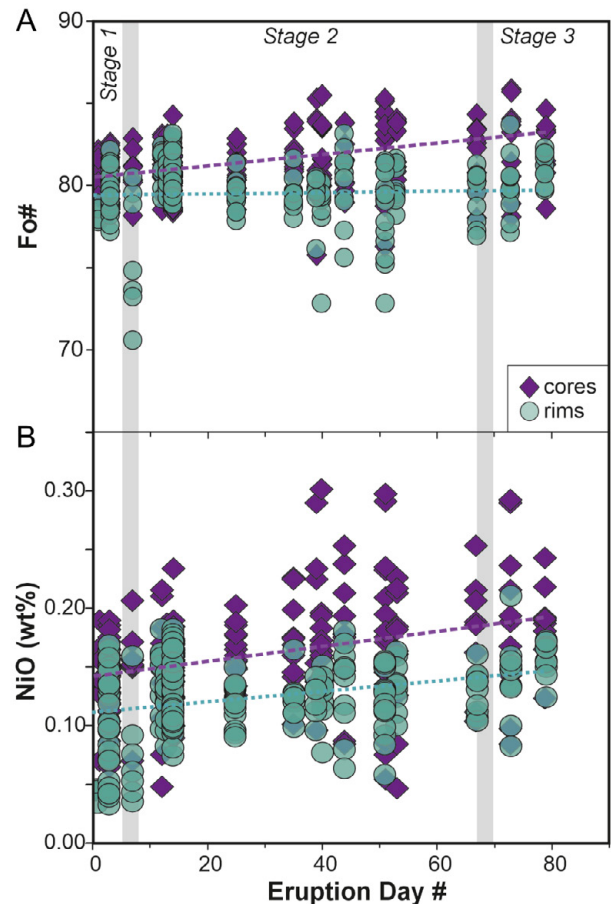


Figure 5: Olivine major element concentrations by core (purple diamonds) and rims (turquoise circles) presented according to eruption time, measured by EPMA. Dashed lines are linear regressions. Stages identified from whole-rock geochemistry [[Scarrow et al. 2024](#)] shown as vertical grey bars. Calculated uncertainties in NiO and Fo are always less than the size of symbols. For full details of precision and accuracy see [Supplementary Material 2](#).

4.4 Thermobarometry

Considering model uncertainty, results of clinopyroxene-liquid geothermobarometry suggest that clinopyroxenes were sourced from magmatic environment(s) in the upper mantle ([Figure 9](#)). Pressure and temperature calculations of clinopyroxene rims and groundmass crystals return mean values of 860 ± 70 (1 σ) MPa and 1128 ± 8 (1 σ) °C, and 786 ± 91 (1 σ) MPa and 1123 ± 8 (1 σ) °C, respectively, following the equilibrium matching approach of [Neave et al. \[2019\]](#), and mean values of 768 ± 72 (1 σ) MPa and 1121 ± 6 (1 σ) °C, and 727 ± 51 (1 σ) MPa and 1115 ± 8 (1 σ) °C, respectively, following the equilibrium matching approach of [MacDonald et al. \[2023\]](#). Regardless of the equilibrium matching approach used, mean pressures and temperatures from these textural populations are within uncertainty of each other once prediction uncertainties associated with model calibrations are considered (1 SEE prediction uncertainties associated with the barometer and thermometer are quoted at 140 MPa and 27 °C, respectively, although

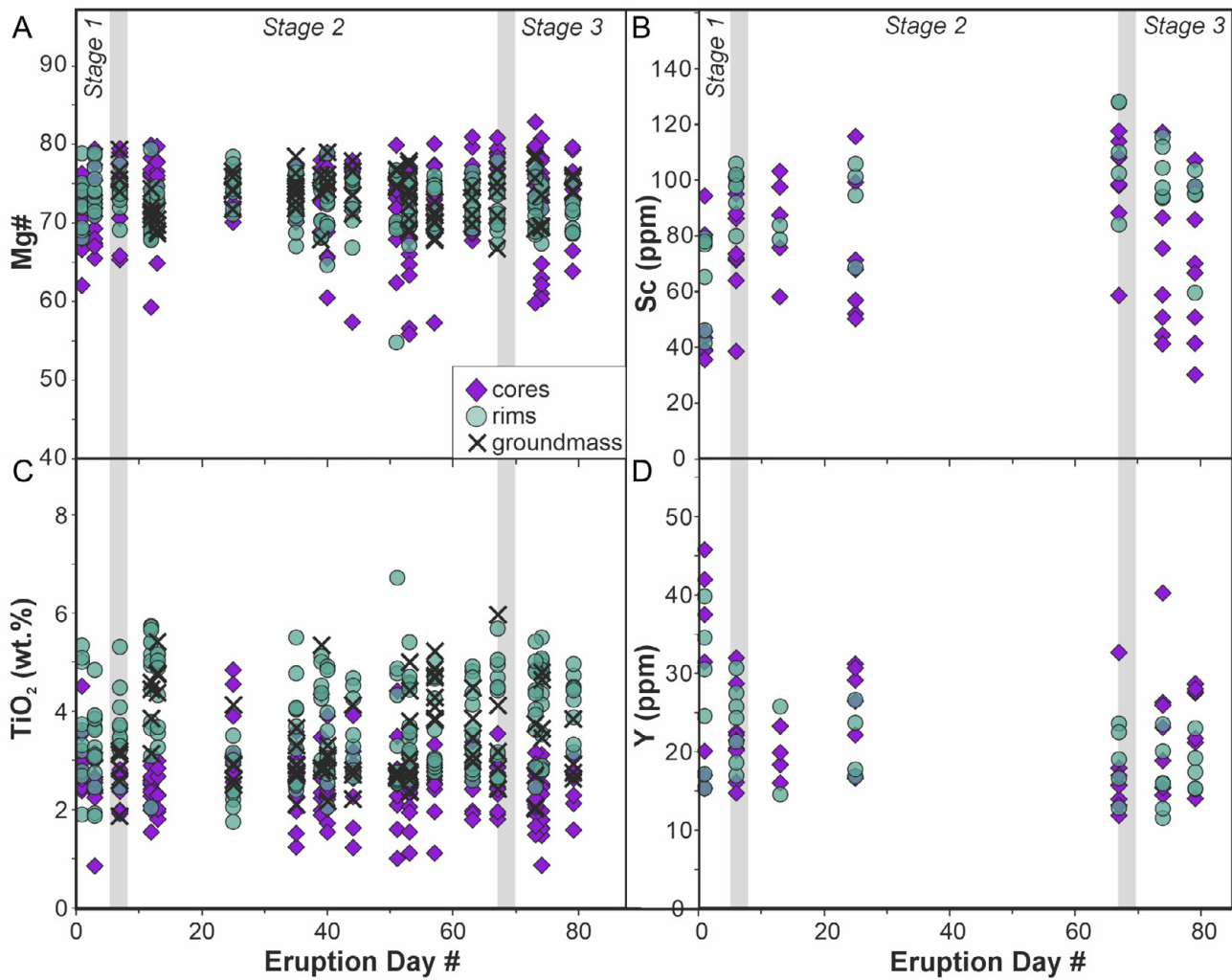


Figure 6: Clinopyroxene major ([A], [C], by EPMA) and trace element ([B], [D], by LA-ICPMS) concentrations grouped by core (purple diamonds), rims (turquoise circles) and groundmass (black crosses) over time. Stages identified from whole-rock geochemistry [Scarrows et al. 2024] shown as vertical grey bars. Calculated 2σ uncertainties in Mg#, TiO₂, Y and Sc are always less than the size of symbols. For full details of precision and accuracy of data see [Supplementary Material 2](#).

the uncertainty could be larger [cf. Wieser et al. 2023]). The range of pressures recorded by clinopyroxene rims also do not change through the course of the eruption. These qualitative observations indicate a continuity of process despite the likely quantitative inaccuracy.

Clinopyroxene cores are chemically and texturally distinct from the rims, being richer in Na at any given Mg#, extend to lower Mg#, and also exhibit less clear evidence of sector zoning (Figure 9A). Where clinopyroxene cores are in chemical equilibrium with glass analyses, they record mean pressures and temperatures of 833 ± 68 (1 σ) MPa and 1127 ± 6 (1 σ) °C, and 833 ± 53 (1 σ) MPa and 1126 ± 8 (1 σ) °C, respectively, following the approaches of Neave et al. [2019] and MacDonald et al. [2023], respectively (Figure 9). Sector zoning plays a clear role in thermobarometric assessments at La Palma—sectors with Al₂O₃ <6.5 wt.% (typically {111}) return systematically lower pressures than clinopyroxene analyses with >6.5 wt.% Al₂O₃ (typical of {hk0}, Figure 9A).

All of the clinopyroxene composition for which we could robustly identify equilibrium liquids returned pressures with a few 10s MPa of ~800 MPa, which corresponds to a depth of ~27 km. Importantly this overlaps with the upper limit of the deeper cluster of depths estimated from melt inclusion and fluid inclusion barometry [Figure 9F; Dayton et al. 2023; 2024]. That is, both clinopyroxene and volatile saturation approaches to barometry at Tajogaite return pressures that are comfortably within uncertainty of each other and confirm the importance of upper mantle magma storage in supplying the eruption.

Amphibole crystals from the earliest phases of the eruption return mean pressures and temperatures of 535 ± 20 (1 σ) MPa and 1043 ± 7 (1 σ) °C. While these values are lower than those estimated from clinopyroxene crystals, pressure values are within 2SEE of values of those estimated clinopyroxene crystals (2SEE uncertainties of amphibole and clinopyroxene barometers are 120 MPa and 280 MPa, respectively). In contrast, amphibole crystals probably do record meaningfully

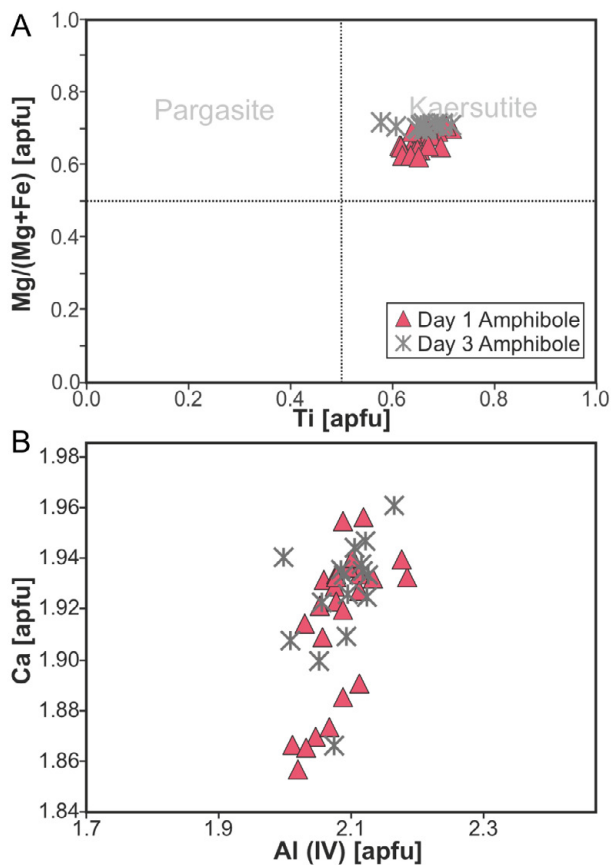


Figure 7: Amphibole major element concentrations measured by EPMA grouped by eruption day: day 1 pink triangles, day 3 grey crosses. Classification follows Leake et al. [1997].

lower temperatures than clinopyroxene textures (2SEE uncertainties of both the amphibole and clinopyroxene thermometers are 27 °C). Indeed, the textural relationships between amphibole and surrounding minerals (see above Section 4.2) suggest amphibole and clinopyroxene could be from different environments, reinforcing the differences in estimated pressures and temperatures.

4.5 Olivine zonation and diffusion chronometry

Textural diversity is observed within olivine macrocrysts despite the variation in core and rim compositions overlapping within individual samples (Figure 5). The abundance of normal, reverse, and unzoned olivine crystals varies throughout the eruption sequence. Systematic changes in olivine textures are observed in tephra samples, and are comparable with the changes observed in the olivine textures in lava samples characterised by QEMSCAN (Figure 4). Stage 1 olivine in tephra is characterised by thin normal zonation (Figure 10A, 10B) with evidence for dissolution in the form of curvilinear crystal edges and widening re-entrants (Figure 10B) in 65 % of the olivine crystals images in day 3 tephra samples. In Stage 2, reverse zoned olivines become apparent, comprising up to 50 % of imaged olivine grains in early Stage 2. This proportion then appears to decrease through Stage 2 and into Stage 3 with un-

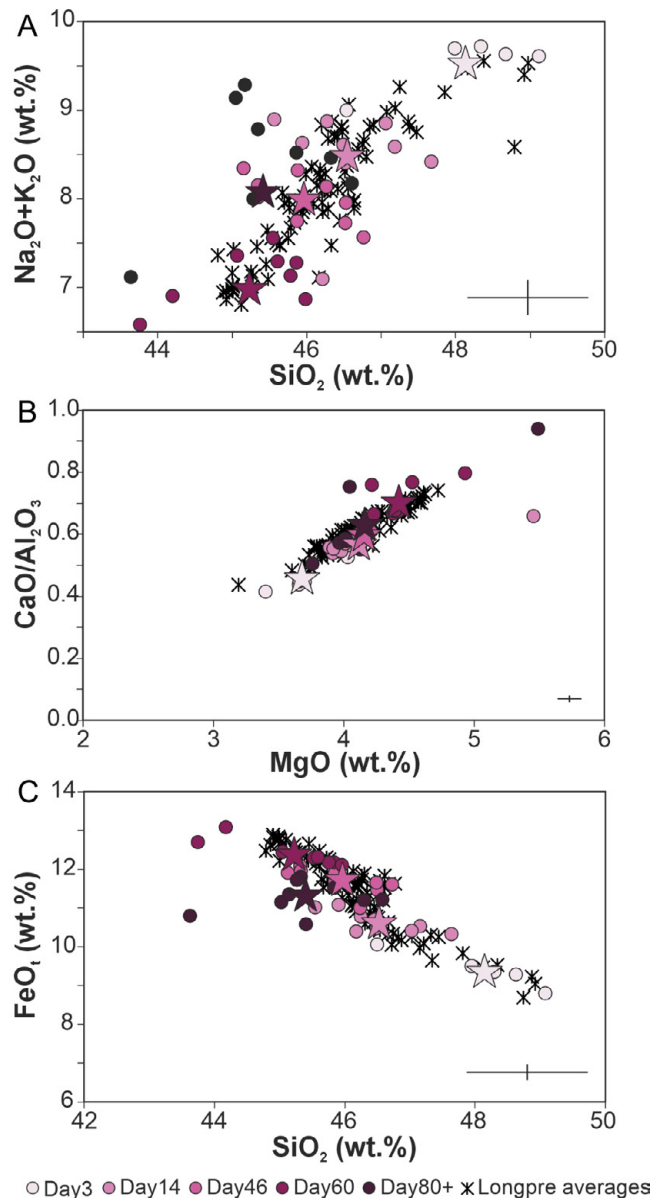


Figure 8: Tephra glass major element concentrations measured by EPMA. Analyses are grouped by eruption day, with lighter colours relating to earlier samples. Individual glass analyses (circles) and their average values (stars) are compared with averages of tephra glass samples (black crosses, Longpré et al. [2025]) throughout the eruption. Black error bars represent uncertainty from standard analyses (see Supplementary Material 2 for details).

zoned grains dominating by day 74 (Figure 10A, 10D). By the end of the eruption, the latest *in situ* tephra have only normal zoned and unzoned olivines, again with >15 % of the studied crystals showing evidence of dissolution ($n = 48$, Figure 10A).

In samples showing olivine zonation, preliminary modelling of timescales for diffusional relaxation was undertaken following the procedures of Chamberlain et al. [2024] (see Section 3 for details of intensive variables used). Only tephra olivines are considered here to minimise the effect of any post-eruptive mineral growth and diffusive relaxation in olivines erupted

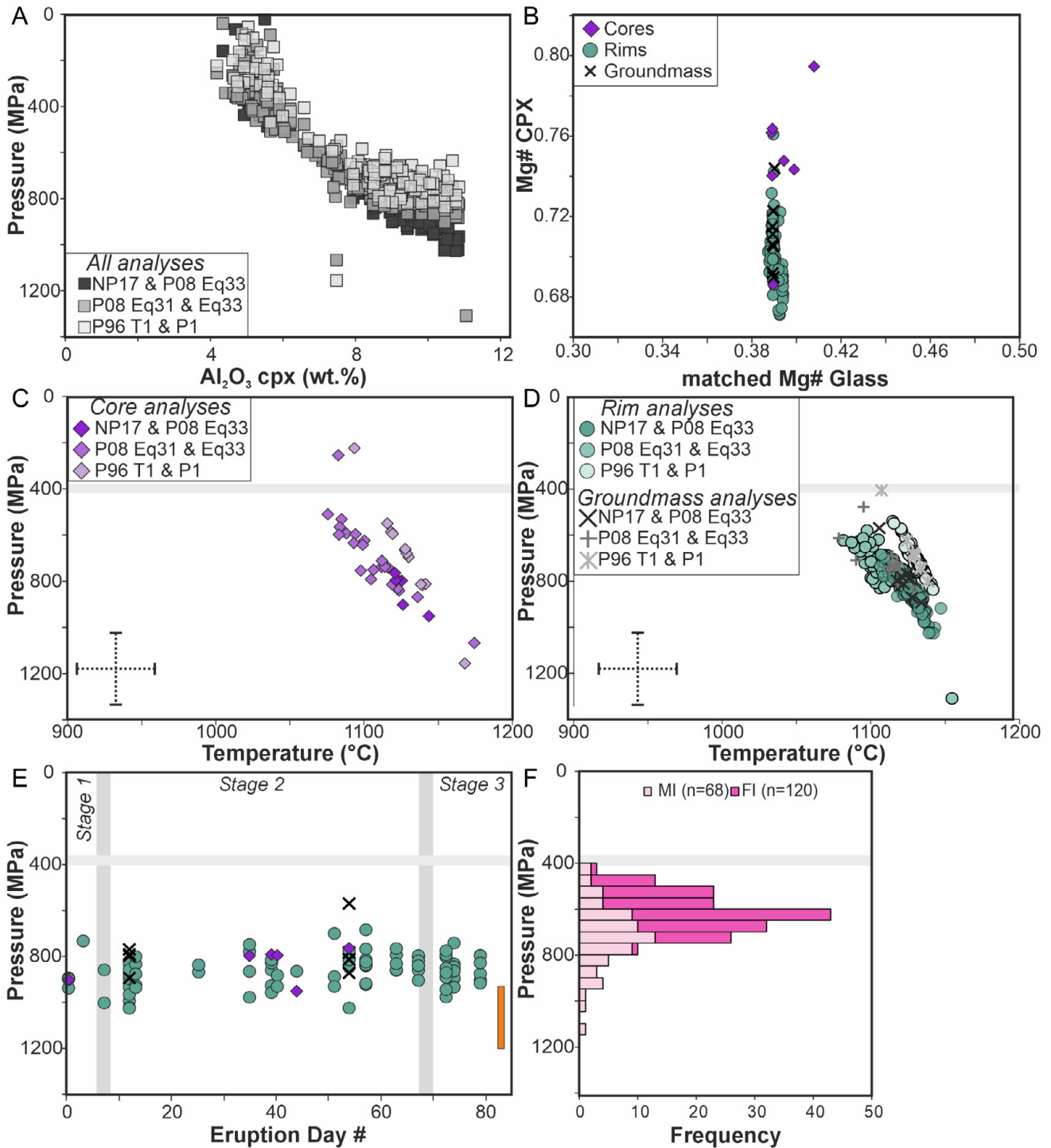


Figure 9: Calculated crystallisation temperatures and pressures for clinopyroxene samples compared with clinopyroxene compositions ([A], highlighting role of sector zoning) and then separated by cores (purple diamonds), rims (green circles) and groundmass (black and grey crosses) from selected samples (Table 1) throughout the eruptive sequence of 2021 Tajogiate eruption, with La Palma pressures for the Moho shown as horizontal light grey bars (after Klügel et al. [2022]). Three different calibrations were run ([A], [C], [D]) on cores, rims and groundmass analyses: Putirka et al. [1996] (P96 T1 & P1), Putirka [2008] (P08, Equation 31 & Equation 33), and Neave and Putirka [2017] for pressures, and Putirka [2008] for temperatures (NP17 & P08 Equation 33). Only the results from application of Neave and Putirka [2017] combined with Putirka [2008] are shown in [B] and [E]. Stages identified from whole-rock geochemistry [Scarrows et al. 2024] shown as vertical grey bars in [E]. Uncertainty on modelled values from propagating analytical uncertainty are shown as dashed crosses ([C], [D]) or an orange bar [E] following Wieser et al. [2023]. Melt inclusion (MI) and fluid inclusion (FI) barometry shown in [F] from Dayton et al. [2023, 2024].

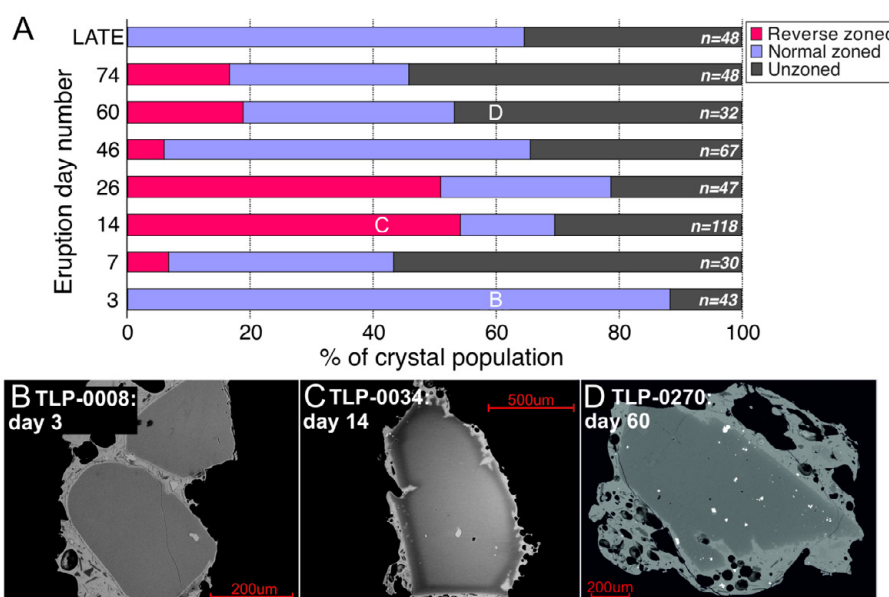


Figure 10: Textural variation of olivine macrocrysts in tephra samples throughout the Tajogaite eruption. [A] shows the proportions of olivine that are reverse-zoned (red), normally-zoned (purple) or unzoned (grey) against the day of the eruption (from 0-85). Number of crystals characterised per sample shown in white italics at the end of each bar. Representative examples of normal [B], reverse-zoned [C] and unzoned [D] macrocrysts are shown in BSE imagery with individual scales on each image. [B] and [D] also display late-stage dissolution textures.

in lava flows [cf. Couperthwaite et al. 2021]. Reverse zoning was modelled from sample TLP-0034 (eruption day 14) on 17 crystals yielding timescales <120 days, with 16 crystals yielding timescales <60 days, at temperatures of 1125 °C (or timescales <80 days, with 16 crystals yielding timescales <40 days, at 1150 °C). If the 14 days since eruption onset is removed, this suggests that these minerals record changes in the magmatic plumbing system occurring in the final few days to weeks prior to eruption (Figure 11). Only core to reverse zone profiles were modelled, as outermost Fe-rich zones cannot be explained by simple 1D diffusion models and are likely a product of decompression-mediated overgrowth during ascent and eruption, which may add a few hours to days to modelled timescales [Romero et al. 2022; Bonechi et al. 2024]. Further work to include the normal-zoned rim, and to determine how consistent the origin of reverse zone timescales are throughout the eruption is necessary to investigate crystal transfer mechanisms [cf. Pankhurst et al. 2018].

5 DISCUSSION

Extensive real-time geophysical, gas geochemical, and environmental monitoring data were collected during the 2021 Tajogaite eruption, but during the eruption no similarly time-resolved mineral-specific petrological data were available, inviting this retrospective study. Three stages have been identified from independent time-series of lava and tephra compositions and magma rheology studies, that coincide with initiation, progression, and waning [see Section 4.1; Day et al. 2022; Ubide et al. 2023; Scarrow et al. 2024; Soldati et al. 2024; Longpré et al. 2025]. The observation that compositional trends correspond to key eruption stages strongly supports the

hypothesis that direct causative relationships exist between the architecture and evolution of magmatic plumbing systems and the behaviour of volcanic eruptions they generate, and, by extension, that these relationships are tractable through detailed petrological study. How these stages relate to the crystal record has not yet been examined systematically. Addressing this gap not only offers the potential to test published interpretations with the benefit of a more complete picture, from which more robust links to other subdisciplines could be made, but also has implications for considering what techniques to apply during future eruptions to generate forecasts of eruptive longevity, and when considering the approaches applied to pre-historic eruptions.

5.1 Generation and storage of Tajogaite magmas

Clinopyroxene is the most abundant, and ubiquitous, mineral phase in the 2021 Tajogaite eruption products (Figure 4). The pressures and temperatures of crystallisation have been calculated by utilising clinopyroxene-melt thermobarometry [Putirka 2008; Neave and Putirka 2017]. Clinopyroxene crystals return mean pressures on the order of 800 MPa (~27 km depth) in broad agreement with other barometry methods from both the 2021 eruption and past eruptions of La Palma (e.g. Ubide et al. [2023], see Scarrow et al. [2024] for full review of depth estimates), and are in line with geophysical estimates of magma storage at La Palma [D'Auria et al. 2022]. Pressures from clinopyroxene cores overlap closely with values obtained from the 1971 eruption of La Palma [Klügel et al. 2005; Barker et al. 2015, of between 410 and 1410 MPa], and indicate that the upper mantle is an important site of magma storage and processing beneath La Palma, as it is be-

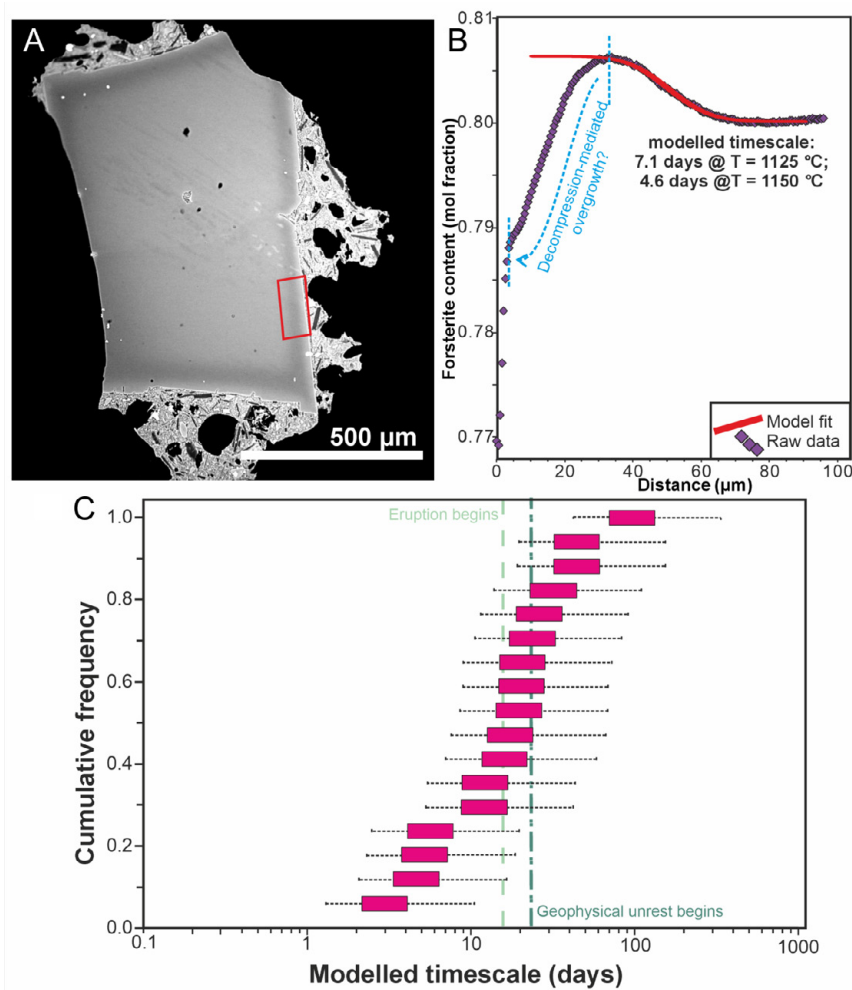


Figure 11: [A] Example of the reverse zoning preserved in olivine macrocrysts, with the area extracted for diffusion (red box) labelled; [B] corresponding Fe-Mg profile for the zone highlighted (purple diamonds), with the modelled fit to the raw data (red line); [C] compiled timescales of Fe-Mg interdiffusion modelling from reverse zones in sample TLP0034 (day 14 tephra). Pink bars represent the systematic uncertainty in timescales based on diffusion at 1125 and 1150 °C. Dashed uncertainty bars represent combined uncertainty at 1 s.d. (see Section 3 for details).

neath many other ocean island systems [Hansteen et al. 1998; Hildner et al. 2012; Kahl et al. 2021; van Gerve et al. 2024]. Furthermore, clinopyroxene barometry indicates that magmas were sourced from the upper mantle throughout the eruption duration. That is, clinopyroxene rims record pressures that remain constant within uncertainty from the very first eruptive products to the last erupted material, suggesting that this deep storage zone plays a key role in driving all stages of the eruption. It is interesting to note that we cannot find evidence of shallower storage in the mineral record of the 2021 eruption, contrary to that found in geophysical studies [e.g. D'Auria et al. 2022] and melt and fluid inclusion work [Sandoval-Velasquez et al. 2023; Dayton et al. 2024; Zanon et al. 2024] where a zone of magma ponding at 6–16 km depth has been inferred.

It has been suggested that the initiation stage (Stage 1, 0–5 days) of the Tajogaite eruption was the result of a deeper magma invading a shallow alkali basalt [Sarrow et al. 2024], that had ponded and crystallised at ~6–16 km [Romero et al. 2022; Fabbri et al. 2023; Bonechi et al. 2024]. Our analyses

of early erupted products do not record these shallower pressures within clinopyroxene crystals, suggesting that whilst the amphiboles erupted in Stage 1 may have formed at shallow pressures, the clinopyroxenes that dominate the erupted crystal assemblage—with the possible exception of their outermost rims that were not captured by our analyses—were sourced from depth (Figure 9). As such, the simplest explanation for our observations is that this magma crystallised clinopyroxene in an upper mantle reservoir before ascending to the shallow storage region where relict crystals could be accumulated.

Clinopyroxene core, rim, and groundmass compositions are remarkably uniform throughout most of the eruption, even though cores are compositionally distinct from rims and groundmass crystals (Figure 6). Moreover, we see no evidence for a slight deepening of magma storage zones tapped during the eruption (cf. Zanon et al. [2024] who suggest a deepening of the magma source region: from 600–750 MPa initially to 590–865 MPa as the eruption progresses) though minor shifts could be masked by the considerable uncertainties associated

with clinopyroxene barometry. Indeed, reducing uncertainties and being able to robustly account for non-equilibrium crystal growth would translate to considerably greater interpretative power in our case. These areas for improvement notwithstanding, it is clear from the combination of the high temporal-resolution data presented here, and other published barometry, the deep source region at ~27 km depth persists throughout the eruption, which has important implications for reconstructing magma plumbing system models.

5.2 Eruption triggering and magma ascent

How long magma is stored in deeper crystallisation zones and what then triggers this magma to ascend and erupt are important questions whose answers may allow improved forecasting of future eruptive activity at La Palma and further afield. Using macrocryst textures and compositions alongside diffusion chronometry timescales yields insights into these processes. Interactions between resident and fresh influxes of magma are thought to have triggered eruptions in many types of systems (e.g. in the 1959 Kilauea Iki episode [Sides et al. 2014]; during the increased explosive phase of eruption from Turrialba 2014–2019 [DeVitre et al. 2019], or the 2018 eruption from Kilauea [Mourey et al. 2023]; also see review in Perugini [2021]). Triggering can occur through increasing the overpressure of a system through volume addition, driving bubble nucleation, or fluxing of volatiles to increase the buoyancy of the melt [Cassidy et al. 2018; Caricchi et al. 2021] for which distinct populations of crystal chemistries in the same eruptive products provide compelling evidence. However, at Tajogaite, the earliest erupted macrocrysts do not have convincing evidence for magma mixing of this kind (i.e. as reverse zones in olivine). Some authors have noted reverse-zoned clinopyroxene in the earliest erupted material [Ubide et al. 2023], yet we observe no evidence for distinct populations of either cores or rims of clinopyroxene which could be attributed to distinct magma sources, and textural quantification of the zoning present is not presented by previous authors.

Instead, early destabilisation towards triggering and evidence for magma mixing are observed in later erupted material from Stage 2 (Figure 2) onwards—although the process began before geophysical detection of unrest (Figure 11). Reverse zonation became the dominant olivine zonation pattern in the first two tephra samples studied in Stage 2 (erupted on day 14 and day 26), suggesting that later erupted material records the influx of more primitive magmas. This signature then wanes through the eruption, before disappearing in the last days of the eruption (CAN_TLP_0445, Figure 10).

Diffusion chronometry focussing upon the timing of initiation of the reverse zones returns timescales on the order of a few days to tens of days prior to eruption onset, with only four of the 17 crystals recording diffusion that initiated after eruption onset (i.e. <14 days at 1125 °C, Figure 11). These timescales overlap with, and extend, the period of climactic unrest detected immediately before the eruption (~7 days of increased seismicity and ground deformation [Carracedo et al. 2022; Civico et al. 2022; Romero et al. 2022; Wadsworth et al. 2022; Suarez et al. 2023]). The overlap between diffusion timescales and timescales of climactic geophysical unrest sug-

gest that both represent the final staging events that record the destabilisation of the magmatic system, which was ultimately triggered to erupt. As the diffusion timescales extend to earlier times than that of immediately pre-eruptive geophysical signals, the process of destabilisation began before its detection by geophysical methods.

Narrow normal (higher Fe) zones with or without evidence of dissolution are present at the very rim of many olivine crystals (Figure 10). These zones cannot be modelled with simple 1D diffusion models, and instead may reflect disequilibrium growth and diffusion on ascent [cf. Couperthwaite et al. 2021]. Detailed combined modelling of these rims (alongside modelling of clinopyroxene zones) in future studies is required to place temporal constraints on this process [e.g. Couperthwaite et al. 2021; 2022; Bell et al. 2023; Kahl et al. 2023], but other studies of ascent during the Tajogaite eruption have suggested ascent of magmas from their storage in the mantle to the surface was of the order of 0.01–0.1 m s⁻¹, with more rapid ascent occurring in the upper crust [Romero et al. 2022; Bonechi et al. 2024; Zanon et al. 2024].

Extended periods of unrest were observed at La Palma for more than four years prior to the 2021 Tajogaite eruption; yet if these relate to magmatic injection and mixing between resident and intruding magmas, then they are not recorded in olivine macrocrysts, which typically lack internal zonation (Figure 10). In contrast, clinopyroxene macrocrysts can exhibit complex zonation (including both oscillatory zoning, and sector zoning in rim domains). It is therefore likely that magmas (and crystal cargos) resided at high temperatures for long enough for evidence for past periods of magma interaction to be eradicated from olivine macrocrysts [cf. Thomson and MacLennan 2013], but preserved in clinopyroxenes, in which the inter-diffusivity of Fe-Mg is approximately three orders of magnitude slower than in olivine at 1125 °C [Dimanov and Sautter 2000; Dohmen and Chakraborty 2007; Couperthwaite et al. 2020].

5.3 Role of crystal cargo in modulating the 2021 Tajogaite eruption composition

Published studies of the 2021 Tajogaite eruption have identified three key stages from either whole-rock analyses [e.g. Scarrow et al. 2024], melt compositions [Longpré et al. 2025], or averaged matrix analyses [Ubide et al. 2023]. By studying the role of the mineral record in defining these stages, we can deconvolve the glass, mineral, and whole-rock record. This will help to understand the processes behind the different eruptive stages, and facilitate developing a strategy for how to use mineralogical data in future eruption monitoring.

The mineral record clearly covaries with the change in eruption products from Stage 1 to Stage 2 (transition occurring over days 5–10) identified from other geochemical analyses [Figure 2, Figure 12 Day et al. 2022; Ubide et al. 2023; Scarrow et al. 2024]. QEMSCAN data of the volumetrically dominant phases illustrate a pre-eruption magmatic plumbing system requiring no more than two crystal assemblage sources: an amphibole-bearing and olivine-poor (and fayalitic) assemblage; and an amphibole-absent and comparatively (forsteritic) olivine rich assemblage. The amphibole-bearing assemblage

was erupted first, but soon after was either exhausted or bypassed by the forsteritic olivine-bearing assemblage, which continued to be erupted until cessation. The earliest erupted lavas and tephra contain a lower abundance of olivine crystals, which are more-evolved (Figure 4), with no evidence for magma mixing in macrocryst phases (Figures 10 and 11), and amphibole as an unstable phase (Figure 7); yet, as discussed above, there is no observable change in the compositions or modelled pressures from clinopyroxene macrocrysts between Stage 1 and Stage 2. The more-evolved glass compositions [Figure 8 Longpré et al. 2025] of tephra from Stage 1, alongside the presence of amphibole, and some comparatively low Fo olivine (Figure 4), substantiate that the first erupted magma was subtly more evolved and more hydrous [Dayton et al. 2024]. Stage 1 products possibly contain components of a residual magma from previous eruptions [Day et al. 2022; Romero et al. 2022; Fabbri et al. 2023; Ubide et al. 2023; Bonechi et al. 2024; Scarrow et al. 2024; Zanon et al. 2024]. The presence of amphibole and low-forsterite olivine together with the potential for the addition of remelted crustal components or remobilised magma explains the more evolved nature of whole-rock composition and variability observed in tephra glass compositions in Stage 1 (Figure 12).

Despite the difference in whole-rock compositions, we see no evidence for compositional changes in clinopyroxene macrocrysts in Stage 1 compared to Stage 2, which requires explanation. If the argument is made for a distinct, older, more evolved and more hydrous magma being erupted from shallower levels at the initiation of the eruption, we must explain why it contains the same clinopyroxene that is present in subsequent fresh and more primitive products from deeper in the system. One answer could be that the clinopyroxene that was erupted early was sourced from the same deep region. This would then imply that this clinopyroxene is residual from previous eruptive/intrusive events together with the rest of the Stage 1 magma because it did not crystallise in the shallow region it retains its deep signature. Why there is no clinopyroxene in Stage 1 that reflects the shallower storage level could be explained by equilibrium growth being suppressed in that environment with amphibole crystallisation at lower temperatures favoured instead. Suppression of clinopyroxene growth in a shallow system or in an ascending magma is consistent with the strong pressure dependence of clinopyroxene stability [e.g. Neave and MacLennan 2020]. The comparatively rapid ascent rates calculated for this eruption and slow diffusivity may have not allowed for clinopyroxene to record the interval between their growth at depth and further crystallisation at final cooling post-eruption, rendering them as largely inactive particles in shallow storage intervals and the active magma. By contrast, olivine and amphibole are faster to respond to the changes in the active magma's intensive parameters (i.e. Fe-Mg interdiffusion and breakdown respectively, see Didonna et al. [2024] and Devine et al. [1998]).

Contrary to the transition from Stage 1 to Stage 2 there is no striking transition from Stage 2 to Stage 3 in the macrocryst assemblage or in macrocryst abundances. There are also no compelling changes in measured mineral compositions, abundances or textures during Stage 3. The petrologi-

cal signal between Stage 2 and 3 is defined by melt [Longpré et al. 2025] and whole-rock [Scarrow et al. 2024] compositions. The more evolved microcryst and rim compositions observed by Ubide et al. [2023] were suggested by those authors to indicate fractionation of the magma source, which they associated with eruption cessation but without a mechanism as to why. We suggest that these evolved microcrysts and rims as may have formed during late-stage ascent and lava emplacement, and so view their more evolved compositions as simply reflective of their more evolved carrier melts [Longpré et al. 2025], rather than indicative of fractionation within the plumbing system at depth. This more-evolved carrier melt has been suggested to have been progressively included in the ascending magma due to collapse of mushy feeder structures [Scarrow et al. 2024], hence the same causative process that liberated the melt caused the shutdown of the eruption (Figure 12).

While this 'shutting down' stage is invisible to the macrocryst crystal cargo itself, the compositional uniformity of the crystal cargo is a critical observation. For instance, should the crystal cargo have changed in character, we would need to account for this and potentially suggest different magma sources, or invoke dynamic fractionation during eruption, and then seek to test these hypotheses with thermometry (we would expect a cooling trend of eruptive temperatures) and/or *in situ* isotopic work to prove the existence of distinct magma batches. Yet the crystal cargo maintaining its character argues strongly against wholesale change in the nature, origin, or number of magma sources. Instead, its consistency reveals the melt to be the agent causing the change, which explains the more subtle change in whole-rock compositions, and leads to an interpretation that includes direct implications for eruption longevity.

5.4 Use of mineralogical information in monitoring eruption progression and cessation

The high temporal resolution of geochemical, geophysical, petrological, and physical volcanology data available for the Tajogaite eruption make this event a useful key to consider what information can be used most effectively to forecast onset, progression, and cessation of future eruptions. Mineralogical data can be more costly to obtain than whole-rock or glass data, and can often require more sample processing (and time) prior to analysis [Re et al. 2021]. However, information about the complexity of magma stalling and ascent pathways are generally only possible from recovering crystal scale histories [e.g. Kahl et al. 2021; Halldórsson et al. 2022; Chamberlain et al. 2024; Weber et al. 2024]. Advances in workflows and methods can allow geochemical data on eruptive products to be obtained much more rapidly and in recent years near-real-time analyses of whole-rock samples and glass have been used to understand eruption progression [e.g. Gansecki et al. 2019; Corsaro and Miraglia 2022; Pankhurst et al. 2022]. Therefore, using mineral-scale information to aid in interpreting whole-rock or melt composition changes are key.

The most important question petrographic study can help to address is how an eruption might evolve and especially when an eruption will end. Scarrow et al. [2024] highlight

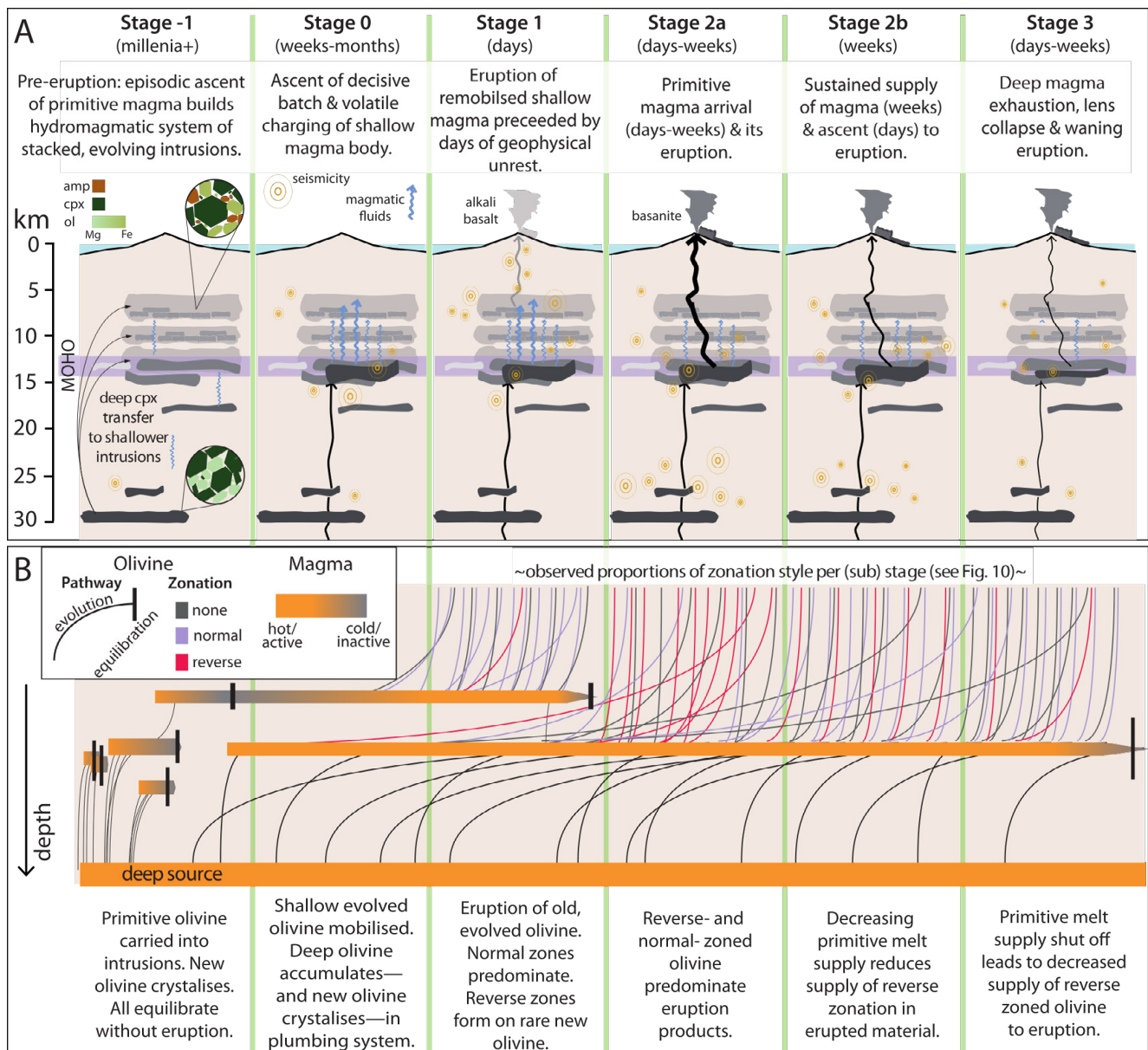


Figure 12: Explanation of olivine zonation populations and diffusion timescale data within the observed eruption phenomenology. Panel [A]: pre-eruption stages of the plumbing system include intrusion of magma carrying deep clinopyroxene, which evolve by olivine and amphibole crystallization at shallow levels, the latter partly due to continued hydration from deep magmatic fluids (Stage -1). Ascent of the primitive magma batch which exsolves the fluids that finally remobilised old magma (Stage 0) and causes the eruption, which then progresses as characterised by [Scarrow et al. \[2024\]](#) in 3 key stages. Panel B: Schematic olivine pathways through the magmatic system. The first olivine to erupt is dominated by normal- and un-zoned populations. Coupled with the low abundance and fayalitic composition ([Figure 4](#)) they correspond to the over-pressured hydrated shallow magma body whose eruption defines Stage 1. The primitive magma ascends during stage 1, interacting with more evolved olivine and causing reverse zones, which dominate the olivine zonation populations in Stage 2a. Diffusion timescales demonstrate a weeks-long period of some interaction in an environment not represented in Stage 1, confirming a spatial-temporal disconnect between magma sources. The proportion of reverse zoned olivine decreases through stage 2a and is absent in the last sample analysed in Stage 3, indicating a waning supply of primitive melt through time.

the importance of the Stage 2–Stage 3 transition as marking the onset of eruption cessation. Additionally, they noted that changes in Tajogaite whole-rock compositions shared similar trends to those observed to precede the cessation of the 2018 Kīlauea and 2021 Fagradalsfjall eruptions, where all three events erupted slightly more-evolved material in the final few

weeks of activity [[Gansecki et al. 2019](#); [Bindeman et al. 2022](#); [Day et al. 2022](#); [Halldórsson et al. 2022](#); [Scarrow et al. 2024](#)]. Yet, being able to link these changes in whole-rock compositions to specific magmatic processes and shutdown of the eruption requires comparison with the mineralogical record, to assess whether the changes reflect varying degrees of crystal

incorporation, varying compositions of mineralogical cargo, or whether the melt composition is changing. Importantly, the macrocryst crystal data collected here, coupled with whole-rock and melt data, show that the mineral cargo (both composition and abundance) does not change at the Stage 2 to Stage 3 transition, therefore suggesting that the feeder system is starting to withdraw remnant melt due to decreased magma flux and related collapse of the magmatic system [Figure 12 Scarrow et al. 2024; Longpré et al. 2025].

In eruptions where the crystal cargo is more dominant and/or more variable, obtaining a reliable melt signature could be more challenging. At Tajogaite the simultaneous and near-continuous eruption of both lava and tephra provided the opportunity to analyse both the melt (tephra glass) without the complications of post-eruption crystallisation, and the magma (lava) without the complications of post-eruption winnowing. The resulting data streams offered intercomparison for the entire duration of the eruption and provided the opportunity to spot covarying and non-co-varying trends, which led to the insights published so far, yet this situation is a rarity in the rock record. These considerations highlight the importance of initial detailed study of erupted products before deciding on the analytical approach for petrological monitoring, and as emphasised by Re et al. [2021] and Scarrow et al. [2024], preparedness in terms of workflows and laboratory agreements are vital to embed petrological monitoring into eruption response methodologies [cf. Gansecki et al. 2019].

5.5 Use of mineralogical information in interpreting past eruptions

By undertaking daily collection of tephra and near-daily collection of lavas in the 2021 Tajogaite eruption, we can interrogate the petrologic record of the eruption and record a time-series evolution of the magma feeding the Tajogaite eruption. In contrast to this approach, sampling of older eruptions is often much more limited than the sampling of recent eruptions, as in many cases the sequence of lava emplacement may be unknown and the temporal relationships between lava and tephra products may not be preserved, at least without some ambiguity. Additionally, financial and/or logistical restrictions may limit the number of samples collected and investigated for a single eruptive sequence. Yet many volcanoes have no historically recorded eruptions, and thus only pre-historic eruptions are available to understand the magmatic plumbing system and eruption progression processes.

How an eruption begins, and what triggers the eruption to begin are key questions in forecasting future eruptive events, yet the mineralogical information presented here highlight that the earliest erupted material does not record a clear or classic trigger and instead shows slightly more-evolved, more diverse and potentially remanent magma being mobilised in the earliest stages of the eruption. The ascent and intrusion of fresher, more primitive magmas (that are likely to have triggered the eruption) are only evident in Stage 2 onwards, with the increased presence of olivine macrocrysts (Figure 4) which show a rapid change to dominantly reverse-zoned textures (Figure 10).

If eruptive product samples from the first ~5 days had not been collected, we may interpret that the intrusion of less-evolved melt interacted directly with stagnant melts, and triggered the eruption. Instead, it appears that a more complex process, where intrusions of more primitive magmas began at least a few weeks before the eruption commenced (Figure 11) and eventually allowed stagnant, more-evolved melts to be erupted, which requires a distinctly different trigger mechanism or mechanisms or response timescale such as fluxing of volatiles or changing crustal stress states [Caricchi et al. 2021]. Often, the very earliest erupted material is immediately covered by subsequent eruptive outputs—indeed the earliest lava sample sites at Tajogaite are now buried beneath later effusions (Figure 1). It is therefore likely that other prehistoric eruptions which do not have the very earliest erupted material preserved or accessible lack the resolution to identify the multi-stage processes responsible for eruption triggering.

Of near equal importance for managing volcanic crises, is understanding how and when an eruption will end; and yet the mineralogical data presented here record no direct evidence for magmatic shutdown (i.e. Stage 2 to Stage 3 boundary). However, identification of transitions to more-evolved whole-rock and melt compositions in the final few days-weeks of multiple historic eruptions [Scarrow et al. 2024] suggests that there are some similar processes occurring (at least in long-lived mafic ocean island eruptions). The identification of this Stage 3 phase at Tajogaite highlights the importance of collecting samples throughout eruptive sequences to understand how magmatic processes and the tapping of different magmas progresses with time.

The identification of discrete phases within long-lived mafic eruptions underscores the importance of careful sampling when studying past eruptions that lack a detailed timeline. Detailed field assessments of the relative timing of samples compared with the range of products from the eruption should be undertaken prior to petrological study. In addition, rapid whole-rock analyses could be carried out to allow future investigators to carefully target advanced mineralogical study on representative samples. In parallel, rapid automated mineralogy techniques (e.g. QEMSCAN®), tuned for application to volcanological products, would provide the complementary data needed to deconvolve the role of crystals and melt in defining the whole-rock composition, and reconcile the signals seen from rapid whole-rock analyses with subvolcanic processes. Ultimately, detailed and thorough study of recent (and well-instrumented) eruptions (alongside future eruptions) will provide the key to interpret the geological record of eruptions, and improve forecasting of future eruption onset, evolution, and cessation.

6 CONCLUSIONS

In this contribution we have integrated a time-series of mineralogical data with existing whole-rock compositional data [Day et al. 2022; Ubide et al. 2023; Scarrow et al. 2024] and compared against timescales of geophysical monitoring data [Civico et al. 2022; D'Auria et al. 2022; Romero et al. 2022; Fabbri et al. 2023] to understand how the 2021 Tajogaite

eruption progressed, with implications for future monitoring of long-lived eruptive events:

1. Measured mineral proportions and compositions are remarkably uniform throughout the 2021 Tajogaite eruptive sequence and important subtle changes could be easily missed without high-frequency sampling. The presence, then absence, of amphibole and changes in olivine (textures, abundance and compositions) are identified at the transition from Stage 1 to Stage 2 of the eruption (over approximately days 5–10), which is interpreted to reflect progressive tapping of more mafic melts that have experienced mixing in the days to weeks prior to eruption onset. Extended application of diffusion chronometry from the Tajogaite crystal record will allow these timescales to be verified and expanded upon.

2. Modelled growth conditions (pressures and temperatures) of clinopyroxene, the dominant macrocryst phase in the 2021 eruption, demonstrate that there is no systematic difference in the depths over which magmas were sourced during the eruption. Calculated pressures of ~800 MPa are in agreement with a deeper (~27 km depth) storage zone in the upper mantle identified from past barometry and geophysical observations of sources of seismicity (see [Scarrow et al. \[2024\]](#) for summary). No mineralogical evidence is found for the previously identified shallower zone of magma storage at ~6–16 km from both seismic, and melt and fluid inclusion studies [[D'Auria et al. 2022](#); [Sandoval-Velasquez et al. 2023](#); [Zanon et al. 2024](#)] of the Tajogaite eruption.

3. No mineralogical changes are observed at the transition from Stage 2 (eruption progression) and Stage 3 (cessation), which was identified from whole-rock and glass analyses [[Scarrow et al. 2024](#); [Longpré et al. 2025](#)]. Hence the variation in whole-rock chemistry (as reported by [Scarrow et al. \[2024\]](#)) is solely a function of changing melt compositions. This observation supports the model of [Scarrow et al. \[2024\]](#) where compaction and collapse of magma storage regions extracts more-evolved melt compositions when the magma supply from depth wanes ([Figure 12](#)), ultimately leading to the end of the eruption.

4. The identification of the transition to Stage 3 at Tajogaite, and the recognition of similar changes in other recent eruptions [[Scarrow et al. 2024](#)] highlights the importance of petrological monitoring in forecasting eruption progression and cessation [e.g. [Ganseccki et al. 2019](#); [Re et al. 2021](#); [Binde-man et al. 2022](#); [Halldórsson et al. 2022](#)]. The mineralogical data collected here highlights that, in fact, whole-rock analyses (chemical and textural) should be the priority when considering which techniques to use in forecasting of eruptive activity in mafic ocean island eruptions. However, further work is needed in more diverse magmatic systems where assembly and evolution of magmas may be more complex than recent eruptions from La Palma, Iceland, and Hawai'i.

AUTHOR CONTRIBUTIONS

KJC, MJP, JHS, DAN, DJM, OAB, JH conceived of the project and secured funding for the study. Samples were collected by

MJP, BCC, JHS, OAB, JH, KJC, AGS, AM-L and FR. MJP, DAN, DJM, SB-F, JG, GKR, PEW, AGS contributed to collecting data and modelling results presented here. KJC wrote the manuscript with support from MJP and DAN. All authors provided critical feedback and helped shape the manuscript.

ACKNOWLEDGEMENTS

This study was made possible by financial support from Natural Environment Research Council (NERC) Urgency grant number: NE/ W007673/1. DAN acknowledges support from NERC (NE/T011106/1). The authors are grateful for the constructive reviews by Teresa Ubide and Geoff Kilgour, alongside the considered editorial handling of Sami Mikhail.

The authors gratefully acknowledge extensive support in the field, including that from: Antonio Álvarez, Alexander G. Stewart, Alba Martín-Lorenzo, Charline Lormand, David Calvo Fernández, Eilish Brennan, Ella Curtis, Ed Llewellyn, Eleazar Padrón, Germán Padilla-Hernández, Germán Cervigón Tomico, Guillermo Recio Sotelo, Ivan Cabrera-Perez, José Barrancos, Jorge Romero, María Asensio Ramos, Pedro Hernández, Rachel Bilsland, Ulrich Keuppens, Victor Ortega Ramos, Nemesio Pérez, William Hernández and Rebecca Winstanley. Finally, the authors express their thanks to David Olivier for rock preparation and additional lab assistance at the University of Manchester.

DATA AVAILABILITY

All data is available as supplementary appendices linked to this manuscript. Datasets are available on the National Geoscience Data Centre: <http://data.bgs.ac.uk/id/dataHolding/13608248>; <http://data.bgs.ac.uk/id/dataHolding/13608284>.

COPYRIGHT NOTICE

© The Author(s) 2025. This article is distributed under the terms of the [Creative Commons Attribution 4.0 International License](#), which permits unrestricted use, distribution, and reproduction in any medium, provided you give appropriate credit to the original author(s) and the source, provide a link to the Creative Commons license, and indicate if changes were made.

REFERENCES

- Allan, A. S. R., D. J. Morgan, C. J. N. Wilson, and M.-A. Millet (2013). "From mush to eruption in centuries: assembly of the super-sized Oruanui magma body". *Contributions to Mineralogy and Petrology* 166(1), pages 143–164. DOI: [10.1007/s00410-013-0869-2](#).
- Barker, A. K., V. R. Troll, J. C. Carracedo, and P. A. Nicholls (2015). "The magma plumbing system for the 1971 Teneguía eruption on La Palma, Canary Islands". *Contributions to Mineralogy and Petrology* 170(5–6). DOI: [10.1007/s00410-015-1207-7](#).
- Bell, S., D. Morgan, K. Joy, J. Pernet-Fisher, and M. Hartley (2023). "Determining the thermal histories of Apollo 15 mare basalts using diffusion modelling in olivine". *Geochimica et Cosmochimica Acta* 357, pages 77–91. DOI: [10.1016/j.gca.2023.08.009](#).

- Bernard, B., M. J. Stock, D. Coppola, S. Hidalgo, M. Bagnardi, S. Gibson, S. Hernandez, P. Ramón, and M. Gleeson (2019). "Chronology and phenomenology of the 1982 and 2015 Wolf volcano eruptions, Galápagos Archipelago". *Journal of Volcanology and Geothermal Research* 374, pages 26–38. DOI: [10.1016/j.jvolgeores.2019.02.013](https://doi.org/10.1016/j.jvolgeores.2019.02.013).
- Bindeman, I. N., F. M. Deegan, V. R. Troll, T. Thordarson, Á. Höskuldsson, W. M. Moreland, E. U. Zorn, A. V. Shevchenko, and T. R. Walter (2022). "Diverse mantle components with invariant oxygen isotopes in the 2021 Fagradalsfjall eruption, Iceland". *Nature Communications* 13(1). DOI: [10.1038/s41467-022-31348-7](https://doi.org/10.1038/s41467-022-31348-7).
- Bonadonna, C., M. Pistolesi, S. Biass, M. Voloschina, J. Romero, D. Coppola, A. Folch, L. D'Auria, A. Martin-Lorenzo, L. Dominguez, C. Pastore, M.-P. Reyes Hardy, and F. Rodríguez (2022). "Physical Characterization of Long-Lasting Hybrid Eruptions: The 2021 Tajogaite Eruption of Cumbre Vieja (La Palma, Canary Islands)". *Journal of Geophysical Research: Solid Earth* 127(11). DOI: [10.1029/2022jb025302](https://doi.org/10.1029/2022jb025302).
- Bonechi, B., M. Polacci, F. Arzilli, J. Romero, J. Fellowes, and M. Burton (2024). "Magma residence time, ascent rate and eruptive style of the November ash-laden activity during the 2021 Tajogaite eruption (La Palma, Spain)". *Volcanica* 7(1), pages 51–65. DOI: [10.30909/vol.07.01.5165](https://doi.org/10.30909/vol.07.01.5165).
- Caricchi, L., M. Townsend, E. Rivalta, and A. Namiki (2021). "The build-up and triggers of volcanic eruptions". *Nature Reviews Earth & Environment* 2(7), pages 458–476. DOI: [10.1038/s43017-021-00174-8](https://doi.org/10.1038/s43017-021-00174-8).
- Carracedo, J. C. (1994). "The Canary Islands: An example of structural control on the growth of large oceanic-island volcanoes". *Journal of Volcanology and Geothermal Research* 60(3–4), pages 225–241. DOI: [10.1016/0377-0273\(94\)90053-1](https://doi.org/10.1016/0377-0273(94)90053-1).
- Carracedo, J. C., E. R. Badiola, H. Guillou, J. De la Nuez, and F. J. Pérez Torrado (2001). "Geology and volcanology of La Palma and El Hierro, Western Canaries". *Estudios Geológicos* 57(5–6), pages 175–273. DOI: [10.3989/egool.01575-6134](https://doi.org/10.3989/egool.01575-6134).
- Carracedo, J. C., S. J. Day, H. Guillou, E. Rodríguez Badiola, J. A. Canas, and F. J. Pérez Torrado (1998). "Hotspot volcanism close to a passive continental margin: the Canary Islands". *Geological Magazine* 135(5), pages 591–604. DOI: [10.1017/s0016756898001447](https://doi.org/10.1017/s0016756898001447).
- Carracedo, J. C., S. J. Day, H. Guillou, and P. Gravestock (1999). "Later stages of volcanic evolution of La Palma, Canary Islands: Rift evolution, giant landslides, and the genesis of the Caldera de Taburiente". *Geological Society of America Bulletin* 111(5), pages 755–768. DOI: [10.1130/0016-7606\(1999\)111<0755:lsoveo>2.3.co;2](https://doi.org/10.1130/0016-7606(1999)111<0755:lsoveo>2.3.co;2).
- Carracedo, J. C. and V. R. Troll (2016). *The Geology of the Canary Islands*. Amsterdam: Elsevier. ISBN: 9780128096635. DOI: [10.1016/c2015-0-04268-x](https://doi.org/10.1016/c2015-0-04268-x).
- Carracedo, J. C., V. R. Troll, J. M. D. Day, H. Geiger, M. Aulinas, V. Soler, F. M. Deegan, F. J. Perez-Torrado, G. Gisbert, E. Gazel, A. Rodriguez-Gonzalez, and H. Albert (2022). "The 2021 eruption of the Cumbre Vieja volcanic ridge on La Palma, Canary Islands". *Geology Today* 38(3), pages 94–107. DOI: [10.1111/gto.12388](https://doi.org/10.1111/gto.12388).
- Cassidy, M., M. Manga, K. Cashman, and O. Bachmann (2018). "Controls on explosive-effusive volcanic eruption styles". *Nature Communications* 9(1). DOI: [10.1038/s41467-018-05293-3](https://doi.org/10.1038/s41467-018-05293-3).
- Chamberlain, K. J., D. J. Morgan, L. E. Lara, R. Walshaw, J. Gardner, S. Chenery, I. L. Millar, and D. Wagner (2024). "Effect of crustal stress state on magmatic stalling and ascent: case study from Puyehue-Cordón Caulle, Chile". *Bulletin of Volcanology* 86(6). DOI: [10.1007/s00445-024-01740-w](https://doi.org/10.1007/s00445-024-01740-w).
- Chamberlain, K. J., D. J. Morgan, and C. J. N. Wilson (2014). "Timescales of mixing and mobilisation in the Bishop Tuff magma body: perspectives from diffusion chronometry". *Contributions to Mineralogy and Petrology* 168(1). DOI: [10.1007/s00410-014-1034-2](https://doi.org/10.1007/s00410-014-1034-2).
- Civico, R., T. Ricci, P. Scarlato, J. Taddeucci, D. Andronico, E. Del Bello, L. D'Auria, P. A. Hernández, and N. M. Pérez (2022). "High-resolution Digital Surface Model of the 2021 eruption deposit of Cumbre Vieja volcano, La Palma, Spain". *Scientific Data* 9(1). DOI: [10.1038/s41597-022-01551-8](https://doi.org/10.1038/s41597-022-01551-8).
- Conway, C. E., K. J. Chamberlain, Y. Harigane, D. J. Morgan, and C. J. Wilson (2020). "Rapid assembly of high-Mg andesites and dacites by magma mixing at a continental arc stratovolcano". *Geology* 48(10), pages 1033–1037. DOI: [10.1130/g47614.1](https://doi.org/10.1130/g47614.1).
- Corsaro, R. A. and L. Miraglia (2022). "Near Real-Time Petrologic Monitoring on Volcanic Glass to Infer Magmatic Processes During the February–April 2021 Paroxysms of the South-East Crater, Etna". *Frontiers in Earth Science* 10. DOI: [10.3389/feart.2022.828026](https://doi.org/10.3389/feart.2022.828026).
- Couperthwaite, F. K., D. J. Morgan, J. Harvey, and M. Kahl (2022). "Pre-eruptive timescales from the historical Hapaimamo eruption at Mauna Loa, Hawai'i". *Journal of Volcanology and Geothermal Research* 432, page 107690. DOI: [10.1016/j.jvolgeores.2022.107690](https://doi.org/10.1016/j.jvolgeores.2022.107690).
- Couperthwaite, F. K., D. J. Morgan, M. J. Pankhurst, P. D. Lee, and J. M. D. Day (2021). "Reducing epistemic and model uncertainty in ionic inter-diffusion chronology: A 3D observation and dynamic modeling approach using olivine from Piton de la Fournaise, La Réunion". *American Mineralogist* 106(3), pages 481–494. DOI: [10.2138/am-2021-7296ccby](https://doi.org/10.2138/am-2021-7296ccby).
- Couperthwaite, F. K., T. Thordarson, D. J. Morgan, J. Harvey, and M. Wilson (2020). "Diffusion Timescales of Magmatic Processes in the Moinui Lava Eruption at Mauna Loa, Hawai'i, as Inferred from Bimodal Olivine Populations". *Journal of Petrology* 61(7). DOI: [10.1093/petrology/egaa058](https://doi.org/10.1093/petrology/egaa058).
- D'Auria, L., I. Koulakov, J. Prudencio, I. Cabrera-Pérez, J. M. Ibáñez, J. Barrancos, R. García-Hernández, D. Martínez van Dorth, G. D. Padilla, M. Przeor, V. Ortega, P. Hernández, and N. M. Pérez (2022). "Rapid magma ascent beneath La Palma revealed by seismic tomography". *Scientific Reports* 12(1). DOI: [10.1038/s41598-022-21818-9](https://doi.org/10.1038/s41598-022-21818-9).
- Day, J. M. D., V. R. Troll, M. Aulinas, F. M. Deegan, H. Geiger, J. C. Carracedo, G. G. Pinto, and F. J. Perez-Torrado (2022). "Mantle source characteristics and magmatic processes during the 2021 La Palma eruption". *Earth and Planetary Sci-*

- ence Letters 597, page 117793. DOI: [10.1016/j.epsl.2022.117793](https://doi.org/10.1016/j.epsl.2022.117793).
- Day, S. J., J. C. Carracedo, H. Guillou, and P. Gravestock (1999). “Recent structural evolution of the Cumbre Vieja volcano, La Palma, Canary Islands: volcanic rift zone reconfiguration as a precursor to volcano flank instability?” *Journal of Volcanology and Geothermal Research* 94(1–4), pages 135–167. DOI: [10.1016/s0377-0273\(99\)00101-8](https://doi.org/10.1016/s0377-0273(99)00101-8).
- Dayton, K., E. Gazel, P. Wieser, V. R. Troll, J. C. Carracedo, M. Aulinas, and F. J. Perez-Torrado (2024). “Magmatic Storage and Volatile Fluxes of the 2021 La Palma Eruption”. *Geochemistry, Geophysics, Geosystems* 25(6). DOI: [10.1029/2024gc011491](https://doi.org/10.1029/2024gc011491).
- Dayton, K., E. Gazel, P. Wieser, V. R. Troll, J. C. Carracedo, H. La Madrid, D. C. Roman, J. Ward, M. Aulinas, H. Geiger, F. M. Deegan, G. Gisbert, and F. J. Perez-Torrado (2023). “Deep magma storage during the 2021 La Palma eruption”. *Science Advances* 9(6). DOI: [10.1126/sciadv.ade7641](https://doi.org/10.1126/sciadv.ade7641).
- Devine, J. D., M. D. Murphy, M. J. Rutherford, J. Barclay, R. S. J. Sparks, M. R. Carroll, S. R. Young, and J. E. Gardner (1998). “Petrologic evidence for pre-eruptive pressure-temperature conditions, and recent reheating, of andesitic magma erupting at the Soufriere Hills Volcano, Montserrat, W.I.” *Geophysical Research Letters* 25(19), pages 3669–3672. DOI: [10.1029/98gl01330](https://doi.org/10.1029/98gl01330).
- DeVitre, C. L., E. Gazel, C. M. Allison, G. Soto, P. Madrigal, G. E. Alvarado, and O. H. Lücke (2019). “Multi-stage chaotic magma mixing at Turrialba volcano”. *Journal of Volcanology and Geothermal Research* 381, pages 330–346. DOI: [10.1016/j.jvolgeores.2019.06.011](https://doi.org/10.1016/j.jvolgeores.2019.06.011).
- Di Fiore, F., A. Vona, A. Scarani, G. Giordano, C. Romano, D. Giordano, L. Caricchi, A. Martin Lorenzo, F. Rodriguez, B. Coldwell, P. Hernandez, and M. Pankhurst (2023). “Experimental Constraints on the Rheology of Lavas From 2021 Cumbre Vieja Eruption (La Palma, Spain)”. *Geophysical Research Letters* 50(4). DOI: [10.1029/2022gl1100970](https://doi.org/10.1029/2022gl1100970).
- Didonna, R., H. Handley, H. Albert, and F. Costa (2024). “Time scales of olivine storage and transport as revealed by diffusion chronometry at Waitomokia Volcanic Complex, Auckland Volcanic Field, New Zealand”. *Journal of Volcanology and Geothermal Research* 451, page 108094. DOI: [10.1016/j.jvolgeores.2024.108094](https://doi.org/10.1016/j.jvolgeores.2024.108094).
- Dimanov, A. and V. Sautter (2000). “Average” interdiffusion of (Fe,Mn)-Mg in natural diopside”. *European Journal of Mineralogy* 12(4), pages 749–760. DOI: [10.1127/0935-1221/2000/0012-0749](https://doi.org/10.1127/0935-1221/2000/0012-0749).
- Dohmen, R. and S. Chakraborty (2007). “Fe–Mg diffusion in olivine II: point defect chemistry, change of diffusion mechanisms and a model for calculation of diffusion coefficients in natural olivine”. *Physics and Chemistry of Minerals* 34(6), pages 409–430. DOI: [10.1007/s00269-007-0158-6](https://doi.org/10.1007/s00269-007-0158-6).
- Fabrizio, A., E. C. Bamber, E. Michailidou, J. E. Romero, F. Arzilli, B. Bonechi, M. Polacci, and M. Burton (2023). “Phase equilibrium experiments and thermodynamic simulations to constrain the pre-eruptive conditions of the 2021 Tajogaite eruption (Cumbre Vieja volcano, La Palma, Canary Islands)”. *Journal of Volcanology and Geothermal Research* 442, page 107901. DOI: [10.1016/j.jvolgeores.2023.107901](https://doi.org/10.1016/j.jvolgeores.2023.107901).
- Fernández, J., J. Escayo, Z. Hu, A. G. Camacho, S. V. Samsonov, J. F. Prieto, K. F. Tiampo, M. Palano, J. J. Mallorquí, and E. Ancochea (2021). “Detection of volcanic unrest onset in La Palma, Canary Islands, evolution and implications”. *Scientific Reports* 11(1). DOI: [10.1038/s41598-021-82292-3](https://doi.org/10.1038/s41598-021-82292-3).
- Frascerria, D., B. Scaillet, J. Andújar, C. Oppenheimer, S. Scaillet, J. Martí, R. Casillas, and C. López (2024). “Experimental constraints on the behaviour of sulphur in the 2021 Cumbre Vieja (La Palma) basanite”. *Journal of Volcanology and Geothermal Research* 456, page 108219. DOI: [10.1016/j.jvolgeores.2024.108219](https://doi.org/10.1016/j.jvolgeores.2024.108219).
- Ganseccki, C., R. L. Lee, T. Shea, S. P. Lundblad, K. Hon, and C. Parcheta (2019). “The tangled tale of Kilauea’s 2018 eruption as told by geochemical monitoring”. *Science* 366(6470). DOI: [10.1126/science.aaz0147](https://doi.org/10.1126/science.aaz0147).
- Geldmacher, J., K. Hoernle, P. Bogaard, S. Duggen, and R. Werner (2005). “New $^{40}\text{Ar}/^{39}\text{Ar}$ age and geochemical data from seamounts in the Canary and Madeira volcanic provinces: Support for the mantle plume hypothesis”. *Earth and Planetary Science Letters* 237(1–2), pages 85–101. DOI: [10.1016/j.epsl.2005.04.037](https://doi.org/10.1016/j.epsl.2005.04.037).
- Global Volcanism Program (GVP) (2025). “Reykjanes (371020)”. *Volcanoes of the World (v. 5.3.1; 6 Aug 2025)*. Edited by E. Venzke. Distributed by Smithsonian Institution. DOI: <https://doi.org/10.5479/si.GVP.VOTW5-2025.5.3>. [Database].
- González-García, D., T. Boulesteix, A. Klügel, and F. Holtz (2023). “Bubble-enhanced basanite-tephrite mixing in the early stages of the Cumbre Vieja 2021 eruption, La Palma, Canary Islands”. *Scientific Reports* 13(1). DOI: [10.1038/s41598-023-41595-3](https://doi.org/10.1038/s41598-023-41595-3).
- Gottlieb, P., G. Wilkie, D. Sutherland, E. Ho-Tun, S. Suthers, K. Perera, B. Jenkins, S. Spencer, A. Butcher, and J. Rayner (2000). “Using quantitative electron microscopy for process mineralogy applications”. *JOM* 52(4), pages 24–25. DOI: [10.1007/s11837-000-0126-9](https://doi.org/10.1007/s11837-000-0126-9).
- Halldórsson, S. A., E. Bali, M. E. Hartley, D. A. Neave, D. W. Peate, G. H. Guðfinnsson, I. Bindeman, M. J. Whitehouse, M. S. Riishuus, G. B. M. Pedersen, S. Jakobsson, R. Askeu, C. R. Gallagher, E. R. Guðmundsdóttir, J. Gudnason, W. M. Moreland, B. V. Óskarsson, P. Nikkola, H. I. Reynolds, J. Schmith, and T. Thordarson (2018). “Petrology and geochemistry of the 2014–2015 Holuhraun eruption, central Iceland: compositional and mineralogical characteristics, temporal variability and magma storage”. *Contributions to Mineralogy and Petrology* 173(8). DOI: [10.1007/s00410-018-1487-9](https://doi.org/10.1007/s00410-018-1487-9).
- Halldórsson, S. A., E. W. Marshall, A. Caracciolo, S. Matthews, E. Bali, M. B. Rasmussen, E. Ranta, J. G. Robin, G. H. Guðfinnsson, O. Sigmarsson, J. MacLennan, M. G. Jackson, M. J. Whitehouse, H. Jeon, Q. H. A. van der Meer, G. K. Mibei, M. H. Kalliokoski, M. M. Repczynska, R. H. Rúnarsdóttir, G. Sigurðsson, M. A. Pfeffer, S. W. Scott, R. Kjartansdóttir, B. I. Kleine, C. Oppenheimer, A. Aiuppa, E. Ilyinskaya, M. Bitetto, G. Giudice, and A. Stefánsson (2022).

- “Rapid shifting of a deep magmatic source at Fagradalsfjall volcano, Iceland”. *Nature* 609(7927), pages 529–534. DOI: [10.1038/s41586-022-04981-x](https://doi.org/10.1038/s41586-022-04981-x).
- Hammer, J., S. Jacob, B. Welsch, E. Hellebrand, and J. Sinton (2016). “Clinopyroxene in postshield Haleakala ankaramite: 1. Efficacy of thermobarometry”. *Contributions to Mineralogy and Petrology* 171(1). DOI: [10.1007/s00410-015-1212-x](https://doi.org/10.1007/s00410-015-1212-x).
- Hansteen, T. H., A. Klügel, and H.-U. Schmincke (1998). “Multi-stage magma ascent beneath the Canary Islands: evidence from fluid inclusions”. *Contributions to Mineralogy and Petrology* 132(1), pages 48–64. DOI: [10.1007/s004100050404](https://doi.org/10.1007/s004100050404).
- Hildner, E., A. Klügel, and T. H. Hansteen (2012). “Barometry of lavas from the 1951 eruption of Fogo, Cape Verde Islands: Implications for historic and prehistoric magma plumbing systems”. *Journal of Volcanology and Geothermal Research* 217–218, pages 73–90. DOI: [10.1016/j.jvolgeores.2011.12.014](https://doi.org/10.1016/j.jvolgeores.2011.12.014).
- Hoernle, K. and H.-U. Schmincke (1993). “The Petrology of the Tholeiites through Melilite Nephelinites on Gran Canaria, Canary Islands: Crystal Fractionation, Accumulation, and Depths of Melting”. *Journal of Petrology* 34(3), pages 573–597. DOI: [10.1093/petrology/34.3.573](https://doi.org/10.1093/petrology/34.3.573).
- Houghton, B. F., W. A. Cockshell, C. E. Gregg, B. H. Walker, K. Kim, C. M. Tisdale, and E. Yamashita (2021). “Land, lava, and disaster create a social dilemma after the 2018 eruption of Kīlauea volcano”. *Nature Communications* 12(1). DOI: [10.1038/s41467-021-21455-2](https://doi.org/10.1038/s41467-021-21455-2).
- Kahl, M., E. Bali, G. H. Guðfinnsson, D. A. Neave, T. Ubide, Q. H. A. van der Meer, and S. Matthews (2021). “Conditions and Dynamics of Magma Storage in the Snæfellsnes Volcanic Zone, Western Iceland: Insights from the Búðahraun and Berserkjahraun Eruptions”. *Journal of Petrology* 62(9). DOI: [10.1093/petrology/egab054](https://doi.org/10.1093/petrology/egab054).
- Kahl, M., E. J. F. Mutch, J. MacLennan, D. J. Morgan, F. Couperthwaite, E. Bali, T. Thordarson, G. H. Guðfinnsson, R. Walshaw, I. Buisman, S. Buhre, Q. H. A. van der Meer, A. Caracciolo, E. W. Marshall, M. B. Rasmussen, C. R. Gallagher, W. M. Moreland, Á. Höskuldsson, and R. A. Askew (2022). “Deep magma mobilization years before the 2021 CE Fagradalsfjall eruption, Iceland”. *Geology* 51(2), pages 184–188. DOI: [10.1130/g50340.1](https://doi.org/10.1130/g50340.1).
- (2023). “Deep magma mobilization years before the 2021 CE Fagradalsfjall eruption, Iceland”. *Geology* 51(2), pages 184–188. DOI: [10.1130/g50340.1](https://doi.org/10.1130/g50340.1).
- Klügel, A. (1998). “Reactions between mantle xenoliths and host magma beneath La Palma (Canary Islands): constraints on magma ascent rates and crustal reservoirs”. *Contributions to Mineralogy and Petrology* 131(2–3), pages 237–257. DOI: [10.1007/s004100050391](https://doi.org/10.1007/s004100050391).
- Klügel, A., E. Albers, and T. H. Hansteen (2022). “Mantle and Crustal Xenoliths in a Tephriphonolite From La Palma (Canary Islands): Implications for Phonolite Formation at Oceanic Island Volcanoes”. *Frontiers in Earth Science* 10. DOI: [10.3389/feart.2022.761902](https://doi.org/10.3389/feart.2022.761902).
- Klügel, A., T. H. Hansteen, and K. Galipp (2005). “Magma storage and underplating beneath Cumbre Vieja volcano, La Palma (Canary Islands)”. *Earth and Planetary Science Letters* 236(1–2), pages 211–226. DOI: [10.1016/j.epsl.2005.04.006](https://doi.org/10.1016/j.epsl.2005.04.006).
- Leake, B. E., A. R. Woolley, C. E. S. Arps, W. D. Birch, M. C. Gilbert, J. D. Grice, F. C. Hawthorne, A. Kato, H. J. Kisch, V. G. Krivovichev, K. Linthout, J. Laird, J. Mandarino, W. V. Maresch, E. H. Nickel, N. M. S. Rock, J. C. Schumacher, D. C. Smith, N. C. N. Stephenson, L. Ungaretti, E. J. W. Whittaker, and G. Youzhi (1997). “Nomenclature of Amphiboles; Report of the Subcommittee on Amphiboles of the International Mineralogical Association Commission on New Minerals and Mineral Names”. *Mineralogical Magazine* 61(405), pages 295–310. DOI: [10.1180/minmag.1997.061.405.13](https://doi.org/10.1180/minmag.1997.061.405.13).
- Longpré, M.-A., S. Tramontano, M. J. Pankhurst, D. C. Roman, M. C. Reiss, F. Cortese, M. R. James, L. Spina, F. Rodríguez, B. Coldwell, A. Martín-Lorenzo, O. Barbee, L. D’Auria, K. J. Chamberlain, and J. H. Scarrow (2025). “Shifting melt composition linked to volcanic tremor at Cumbre Vieja volcano”. *Nature Geoscience* 18(2), pages 175–183. DOI: [10.1038/s41561-024-01623-x](https://doi.org/10.1038/s41561-024-01623-x).
- MacDonald, A., T. Ubide, S. Mollo, A. Pontesilli, and M. Massotta (2023). “The Influence of Undercooling and Sector Zoning on Clinopyroxene–Melt Equilibrium and Thermobarometry”. *Journal of Petrology* 64(10). DOI: [10.1093/petrology/egad074](https://doi.org/10.1093/petrology/egad074).
- Mangler, M. F., C. M. Petrone, and J. Prytulak (2022). “Magma recharge patterns control eruption styles and magnitudes at Popocatepetl volcano (Mexico)”. *Geology* 50(3), pages 366–370. DOI: [10.1130/g49365.1](https://doi.org/10.1130/g49365.1).
- Matthews, S. W., A. Caracciolo, E. Bali, S. A. Halldórsson, O. Sigmarsson, G. H. Guðfinnsson, G. B. M. Pedersen, J. G. Robin, E. W. Marshall, A. A. Aden, B. Ý. Gísladóttir, C. Bosq, D. Auclair, H. Merrill, N. Levillayer, N. Löw, R. H. Rúnarsdóttir, S. M. Johnson, S. Steinþórsson, and V. Drouin (2024). “A dynamic mid-crustal magma domain revealed by the 2023 to 2024 Sundhnúksíggar eruptions in Iceland”. *Science* 386(6719), pages 309–314. DOI: [10.1126/science.adp8778](https://doi.org/10.1126/science.adp8778).
- Meredith, E. S., S. F. Jenkins, J. L. Hayes, D. Lallemand, N. I. Deligne, and N. R. X. Teng (2024). “Lava flow impacts on the built environment: insights from a new global dataset”. *Journal of Applied Volcanology* 13(1). DOI: [10.1186/s13617-023-00140-7](https://doi.org/10.1186/s13617-023-00140-7).
- Mollo, S., K. Putirka, V. Misiti, M. Soligo, and P. Scarlato (2013). “A new test for equilibrium based on clinopyroxene–melt pairs: Clues on the solidification temperatures of Etnean alkaline melts at post-eruptive conditions”. *Chemical Geology* 352, pages 92–100. DOI: [10.1016/j.chemgeo.2013.05.026](https://doi.org/10.1016/j.chemgeo.2013.05.026).
- Morgan, D. and S. Blake (2006). “Magmatic residence times of zoned phenocrysts: introduction and application of the binary element diffusion modelling (BEDM) technique”. *Contributions to Mineralogy and Petrology* 151(1), pages 58–70. DOI: [10.1007/s00410-005-0045-4](https://doi.org/10.1007/s00410-005-0045-4).
- Mourey, A. J., T. Shea, F. Costa, B. Shiro, and R. J. Longman (2023). “Years of magma intrusion primed Kilauea Volcano (Hawai’i) for the 2018 eruption: evidence from olivine dif-

- fusion chronometry and monitoring data". *Bulletin of Volcanology* 85(3). DOI: [10.1007/s00445-023-01633-4](https://doi.org/10.1007/s00445-023-01633-4).
- Neave, D. A., E. Bali, G. H. Guðfinnsson, S. A. Halldórsson, M. Kahl, A.-S. Schmidt, and F. Holtz (2019). "Clinopyroxene–Liquid Equilibria and Geothermobarometry in Natural and Experimental Tholeiites: the 2014–2015 Holuhraun Eruption, Iceland". *Journal of Petrology* 60(8), pages 1653–1680. DOI: [10.1093/petrology/egz042](https://doi.org/10.1093/petrology/egz042).
- Neave, D. A. and J. MacLennan (2020). "Clinopyroxene Dissolution Records Rapid Magma Ascent". *Frontiers in Earth Science* 8. DOI: [10.3389/feart.2020.00188](https://doi.org/10.3389/feart.2020.00188).
- Neave, D. A., J. MacLennan, M. Edmonds, and T. Thordarson (2014). "Melt mixing causes negative correlation of trace element enrichment and CO₂ content prior to an Icelandic eruption". *Earth and Planetary Science Letters* 400, pages 272–283. DOI: [10.1016/j.epsl.2014.05.050](https://doi.org/10.1016/j.epsl.2014.05.050).
- Neave, D. A. and K. D. Putirka (2017). "A new clinopyroxene-liquid barometer, and implications for magma storage pressures under Icelandic rift zones". *American Mineralogist* 102(4), pages 777–794. DOI: [10.2138/am-2017-5968](https://doi.org/10.2138/am-2017-5968).
- Ostorero, L., H. Balcone-Boissard, G. Boudon, N. M. Shapiro, A. Belousov, M. Belousova, A. Auer, S. L. Senyukov, and S. Y. Droznina (2022). "Correlated petrology and seismicity indicate rapid magma accumulation prior to eruption of Kizimen volcano, Kamchatka". *Communications Earth & Environment* 3(1). DOI: [10.1038/s43247-022-00622-3](https://doi.org/10.1038/s43247-022-00622-3).
- Padrón, E., N. M. Pérez, P. A. Hernández, H. Sumino, G. V. Melián, M. Alonso, F. Rodríguez, M. Asensio-Ramos, and L. D'Auria (2022). "Early Precursory Changes in the ³He/⁴He Ratio Prior to the 2021 Tajogaite Eruption at Cumbre Vieja Volcano, La Palma, Canary Islands". *Geophysical Research Letters* 49(18). DOI: [10.1029/2022gl099992](https://doi.org/10.1029/2022gl099992).
- Pankhurst, M. J., N. Gueninchault, M. Andrew, and E. Hill (2019). "Non-destructive three-dimensional crystallographic orientation analysis of olivine using laboratory diffraction contrast tomography". *Mineralogical Magazine* 83(5), pages 705–711. DOI: [10.1180/mgm.2019.51](https://doi.org/10.1180/mgm.2019.51).
- Pankhurst, M. J., D. J. Morgan, T. Thordarson, and S. C. Loughlin (2018). "Magmatic crystal records in time, space, and process, causatively linked with volcanic unrest". *Earth and Planetary Science Letters* 493, pages 231–241. DOI: [10.1016/j.epsl.2018.04.025](https://doi.org/10.1016/j.epsl.2018.04.025).
- Pankhurst, M. J., J. H. Scarrow, O. A. Barbee, J. Hickey, B. C. Coldwell, G. K. Rollinson, J. A. Rodríguez-Losada, A. Martín Lorenzo, F. Rodríguez, W. Hernández, D. Calvo Fernández, P. A. Hernández, and N. M. Pérez (2022). "Rapid response petrology for the opening eruptive phase of the 2021 Cumbre Vieja eruption, La Palma, Canary Islands". *Volcanica* 5(1), pages 1–10. DOI: [10.30909/vol.05.01.0110](https://doi.org/10.30909/vol.05.01.0110).
- Paton, C., J. Hellstrom, B. Paul, J. Woodhead, and J. Hergt (2011). "Iolite: Freeware for the visualisation and processing of mass spectrometric data". *Journal of Analytical Atomic Spectrometry* 26(12), page 2508. DOI: [10.1039/c1ja10172b](https://doi.org/10.1039/c1ja10172b).
- Perugini, D. (2021). "Magma Mixing: The Trigger for Explosive Volcanic Eruptions". *The Mixing of Magmas*. Springer International Publishing, pages 135–148. ISBN: 9783030818111. DOI: [10.1007/978-3-030-81811-1_10](https://doi.org/10.1007/978-3-030-81811-1_10).
- Piña-Varas, P., J. Ledo, P. Queralt, D. M. van Dorth, A. Marcuello, I. Cabrera-Pérez, L. D'Auria, and A. Martí (2023). "Volcanic monitoring of the 2021 La Palma eruption using long-period magnetotelluric data". *Scientific Reports* 13(1). DOI: [10.1038/s41598-023-43326-0](https://doi.org/10.1038/s41598-023-43326-0).
- Pirrie, D. and G. K. Rollinson (2011). "Unlocking the applications of automated mineral analysis". *Geology Today* 27(6), pages 226–235. DOI: [10.1111/j.1365-2451.2011.00818.x](https://doi.org/10.1111/j.1365-2451.2011.00818.x).
- Pizarro, C., M. A. Parada, C. Contreras, and E. Morgado (2019). "Cryptic magma recharge associated with the most voluminous 20th century eruptions (1921, 1948 and 1971) at Villarrica Volcano". *Journal of Volcanology and Geothermal Research* 384, pages 48–63. DOI: [10.1016/j.jvolgeores.2019.07.001](https://doi.org/10.1016/j.jvolgeores.2019.07.001).
- Poland, M. P., A. Miklius, and E. K. Montgomery-Brown (2008). "Magma supply, storage, and transport at shield-stage Hawaiian volcanoes". *Characteristics of Hawaiian volcanoes*. Edited by M. P. Poland, T. J. Takahashi, and C. M. Landowski. Volume 1801. Reston, Virginia: U.S. Geological Survey. Chapter 5, pages 179–234. DOI: [10.3133/pp18015](https://doi.org/10.3133/pp18015). U.S. Geological Survey Professional paper 1801-5.
- Prägel, N.-O. and P. Holm (2006). "Lithospheric contributions to high-MgO basanites from the Cumbre Vieja Volcano, La Palma, Canary Islands and evidence for temporal variation in plume influence". *Journal of Volcanology and Geothermal Research* 149(3–4), pages 213–239. DOI: [10.1016/j.jvolgeores.2005.07.019](https://doi.org/10.1016/j.jvolgeores.2005.07.019).
- Putirka, K. D. (2008). "Thermometers and Barometers for Volcanic Systems". *Reviews in Mineralogy and Geochemistry* 69(1), pages 61–120. DOI: [10.2138/rmg.2008.69.3](https://doi.org/10.2138/rmg.2008.69.3).
- Putirka, K. D., M. Johnson, R. Kinzler, J. Longhi, and D. Walker (1996). "Thermobarometry of mafic igneous rocks based on clinopyroxene-liquid equilibria, 0–30 kbar". *Contributions to Mineralogy and Petrology* 123(1), pages 92–108. DOI: [10.1007/s004100050145](https://doi.org/10.1007/s004100050145).
- Re, G., R. A. Corsaro, C. D'Amico, and M. Pompilio (2021). "Petrological monitoring of active volcanoes: A review of existing procedures to achieve best practices and operative protocols during eruptions". *Journal of Volcanology and Geothermal Research* 419, page 107365. DOI: [10.1016/j.jvolgeores.2021.107365](https://doi.org/10.1016/j.jvolgeores.2021.107365).
- Ridolfi, F. (2021). "Amp-TB2: An Updated Model for Calcic Amphibole Thermobarometry". *Minerals* 11(3), page 324. DOI: [10.3390/min11030324](https://doi.org/10.3390/min11030324).
- Ridolfi, F. and A. Renzulli (2012). "Calcic amphiboles in calc-alkaline and alkaline magmas: thermobarometric and chemometric empirical equations valid up to 1,130°C and 2.2 GPa". *Contributions to Mineralogy and Petrology* 163(5), pages 877–895. DOI: [10.1007/s00410-011-0704-6](https://doi.org/10.1007/s00410-011-0704-6).
- Rollinson, G. K., J. C. Andersen, R. J. Stickland, M. Boni, and R. Fairhurst (2011). "Characterisation of non-sulphide zinc deposits using QEMSCAN®". *Minerals Engineering* 24(8), pages 778–787. DOI: [10.1016/j.mineng.2011.02.004](https://doi.org/10.1016/j.mineng.2011.02.004).
- Romero, J. E., M. Burton, F. Cáceres, J. Taddeucci, R. Civico, T. Ricci, M. J. Pankhurst, P. A. Hernández, C. Bonadonna, E. W. Llewellyn, M. Pistolesi, M. Polacci, C. Solana, L. D'Auria, F. Arzilli, D. Andronico, F. Rodríguez, M. Asensio-Ramos,

- A. Martín-Lorenzo, C. Hayer, P. Scarlato, and N. M. Perez (2022). "The initial phase of the 2021 Cumbre Vieja ridge eruption (Canary Islands): Products and dynamics controlling edifice growth and collapse". *Journal of Volcanology and Geothermal Research* 431, page 107642. DOI: [10.1016/j.jvolgeores.2022.107642](https://doi.org/10.1016/j.jvolgeores.2022.107642).
- Ruth, D. C. S. and F. Costa (2021). "A petrological and conceptual model of Mayon volcano (Philippines) as an example of an open-vent volcano". *Bulletin of Volcanology* 83(10). DOI: [10.1007/s00445-021-01486-9](https://doi.org/10.1007/s00445-021-01486-9).
- Sandoval-Velasquez, A., A. Rizzo, F. Casetta, T. Ntaflou, A. Aiuppa, M. Alonso, E. Padrón, M. Pankhurst, A. Mundl-Petermeier, V. Zanon, and N. Pérez (2023). "The noble gas signature of the 2021 Tajogaite eruption (La Palma, Canary Islands)". *Journal of Volcanology and Geothermal Research* 443, page 107928. DOI: [10.1016/j.jvolgeores.2023.107928](https://doi.org/10.1016/j.jvolgeores.2023.107928).
- Scarrow, J. H., M. J. Pankhurst, O. A. Barbee, K. J. Chamberlain, D. J. Morgan, M.-A. Longpré, S. Tramontano, J. Hickey, D. A. Neave, G. K. Rollinson, A. G. Stewart, P. E. Wieser, B. C. Coldwell, W. Hernández, L. D'Auria, and N. M. Pérez (2024). "Decoding links between magmatic processes and eruption dynamics: whole-rock time series petrology of the 2021 Tajogaite eruption, La Palma". *Volcanica* 7(2), pages 953–980. DOI: [10.30909/vol.07.02.953980](https://doi.org/10.30909/vol.07.02.953980).
- Schmincke, H.-U., A. Klügel, T. H. Hansteen, K. Hoernle, and P. van den Bogaard (1998). "Samples from the Jurassic ocean crust beneath Gran Canaria, La Palma and Lanzarote (Canary Islands)". *Earth and Planetary Science Letters* 163(1–4), pages 343–360. DOI: [10.1016/S0012-821X\(98\)00168-X](https://doi.org/10.1016/S0012-821X(98)00168-X).
- Sides, I., M. Edmonds, J. MacLennan, B. Houghton, D. Swanson, and M. Steele-MacInnis (2014). "Magma mixing and high fountaining during the 1959 Kilauea Iki eruption, Hawaii". *Earth and Planetary Science Letters* 400, pages 102–112. DOI: [10.1016/j.epsl.2014.05.024](https://doi.org/10.1016/j.epsl.2014.05.024).
- Soldati, A., C. Cimarelli, U. Kueppers, F. Cáceres, D. Müller, M. Pankhurst, J. H. Scarrow, N. Perez, and D. B. Dingwell (2024). "Melt viscosity tracks the volcanic and magmatic evolution of the 2021 Tajogaite eruption, La Palma (Canary Islands)". *Journal of Volcanology and Geothermal Research* 455, page 108210. DOI: [10.1016/j.jvolgeores.2024.108210](https://doi.org/10.1016/j.jvolgeores.2024.108210).
- Staudigel, H., G. Feraud, and G. Giannerini (1986). "The history of intrusive activity on the island of La Palma (Canary Islands)". *Journal of Volcanology and Geothermal Research* 27(3–4), pages 299–322. DOI: [10.1016/0377-0273\(86\)90018-1](https://doi.org/10.1016/0377-0273(86)90018-1).
- Streck, M. J. (2008). "Mineral Textures and Zoning as Evidence for Open System Processes". *Reviews in Mineralogy and Geochemistry* 69(1), pages 595–622. DOI: [10.2138/rmg.2008.69.15](https://doi.org/10.2138/rmg.2008.69.15).
- Suarez, E., I. Domínguez-Cerdeña, A. Villaseñor, S. S.-M. Aparicio, C. del Fresno, and L. García-Cañada (2023). "Unveiling the pre-eruptive seismic series of the La Palma 2021 eruption: Insights through a fully automated analysis". *Journal of Volcanology and Geothermal Research* 444, page 107946. DOI: [10.1016/j.jvolgeores.2023.107946](https://doi.org/10.1016/j.jvolgeores.2023.107946).
- Taddeucci, J., P. Scarlato, D. Andronico, T. Ricci, R. Civico, E. Del Bello, L. Spina, L. D'Auria, M. Asensio-Ramos, D. Calvo, E. Padrón, P. A. Hernández, and N. M. Pérez (2023). "The Explosive Activity of the 2021 Tajogaite Eruption (La Palma, Canary Islands, Spain)". *Geochemistry, Geophysics, Geosystems* 24(6). DOI: [10.1029/2023gc010946](https://doi.org/10.1029/2023gc010946).
- Thomson, A. and J. MacLennan (2013). "The Distribution of Olivine Compositions in Icelandic Basalts and Picrites". *Journal of Petrology* 54(4), pages 745–768. DOI: [10.1093/petrology/egs083](https://doi.org/10.1093/petrology/egs083).
- Thordarson, T. and G. Larsen (2007). "Volcanism in Iceland in historical time: Volcano types, eruption styles and eruptive history". *Journal of Geodynamics* 43(1), pages 118–152. DOI: [10.1016/j.jog.2006.09.005](https://doi.org/10.1016/j.jog.2006.09.005).
- Torres-González, P., N. Luengo-Oroz, H. Lamolda, W. D'Alessandro, H. Albert, I. Iribarren, D. Moure-García, and V. Soler (2020). "Unrest signals after 46 years of quiescence at Cumbre Vieja, La Palma, Canary Islands". *Journal of Volcanology and Geothermal Research* 392, page 106757. DOI: [10.1016/j.jvolgeores.2019.106757](https://doi.org/10.1016/j.jvolgeores.2019.106757).
- Ubide, T., Á. Márquez, E. Ancochea, M. J. Huertas, R. Herrera, J. J. Coello-Bravo, D. Sanz-Mangas, J. Mulder, A. MacDonald, and I. Galindo (2023). "Discrete magma injections drive the 2021 La Palma eruption". *Science Advances* 9(27). DOI: [10.1126/sciadv.adg4813](https://doi.org/10.1126/sciadv.adg4813).
- Ubide, T., S. Mollo, J.-x. Zhao, M. Nazzari, and P. Scarlato (2019). "Sector-zoned clinopyroxene as a recorder of magma history, eruption triggers, and ascent rates". *Geochimica et Cosmochimica Acta* 251, pages 265–283. DOI: [10.1016/j.gca.2019.02.021](https://doi.org/10.1016/j.gca.2019.02.021).
- Van Gerve, T. D., D. A. Neave, P. Wieser, H. Lamadrid, N. Hulsbosch, and O. Namur (2024). "The Origin and Differentiation of CO₂-Rich Primary Melts in Ocean Island Volcanoes: Integrating 3D X-Ray Tomography with Chemical Microanalysis of Olivine-Hosted Melt Inclusions from Pico (Azores)". *Journal of Petrology* 65(2). DOI: [10.1093/petrology/egae006](https://doi.org/10.1093/petrology/egae006).
- Wadsworth, F. B., E. W. Llewellyn, J. I. Farquharson, J. K. Gillies, A. Loisel, L. Frey, E. Ilyinskaya, T. Thordarson, S. Tramontano, E. Lev, M. J. Pankhurst, A. G. Rull, M. Asensio-Ramos, N. M. Pérez, P. A. Hernández, D. Calvo, M. C. Solana, U. Kueppers, and A. P. Santabárbara (2022). "Crowd-sourcing observations of volcanic eruptions during the 2021 Fagradalsfjall and Cumbre Vieja events". *Nature Communications* 13(1). DOI: [10.1038/s41467-022-30333-4](https://doi.org/10.1038/s41467-022-30333-4).
- Weber, G., J. Blundy, J. Barclay, D. M. Pyle, P. Cole, H. Frey, M. Manon, B. V. Davies, and K. Cashman (2024). "Petrology of the 2020–21 effusive to explosive eruption of La Soufrière Volcano, St Vincent: insights into plumbing system architecture and magma assembly mechanism". *Geological Society, London, Special Publications* 539(1), pages 171–200. DOI: [10.1144/sp539-2022-177](https://doi.org/10.1144/sp539-2022-177).
- Weis, F. A., H. Skogby, V. R. Troll, F. M. Deegan, and B. Dahren (2015). "Magmatic water contents determined through clinopyroxene: Examples from the Western Canary Islands, Spain". *Geochemistry, Geophysics, Geosystems* 16(7), pages 2127–2146. DOI: [10.1002/2015gc005800](https://doi.org/10.1002/2015gc005800).

- Wieser, P. E., M. L. M. Gleeson, S. Matthews, C. DeVitre, and E. Gazel (2025). “Determining the pressure-temperature-composition (P-T-X) conditions of magma storage”. *Treatise on Geochemistry*. Elsevier, pages 83–151. ISBN: 9780323997638. DOI: [10.1016/b978-0-323-99762-1.00024-3](https://doi.org/10.1016/b978-0-323-99762-1.00024-3).
- Wieser, P. E., A. J. R. Kent, C. B. Till, J. Donovan, D. A. Neave, D. L. Blatter, and M. J. Krawczynski (2023). “Barometers Behaving Badly I: Assessing the Influence of Analytical and Experimental Uncertainty on Clinopyroxene Thermobarometry Calculations at Crustal Conditions”. *Journal of Petrology* 64(2). DOI: [10.1093/petrology/egac126](https://doi.org/10.1093/petrology/egac126).
- Wieser, P. E., M. Petrelli, J. Lubbers, E. Wieser, S. Ozaydin, A. Kent, and C. Till (2022). “Thermobar: An open-source Python3 tool for thermobarometry and hygrometry”. *Volcanica* 5(2), pages 349–384. DOI: [10.30909/vol.05.02.349384](https://doi.org/10.30909/vol.05.02.349384).
- Zanon, V., L. Dâ€™Auria, F. Schiavi, K. Cyrzan, and M. J. Pankhurst (2024). “Toward a near real-time magma ascent monitoring by combined fluid inclusion barometry and ongoing seismicity”. *Science Advances* 10(6). DOI: [10.1126/sciadv.adi4300](https://doi.org/10.1126/sciadv.adi4300).